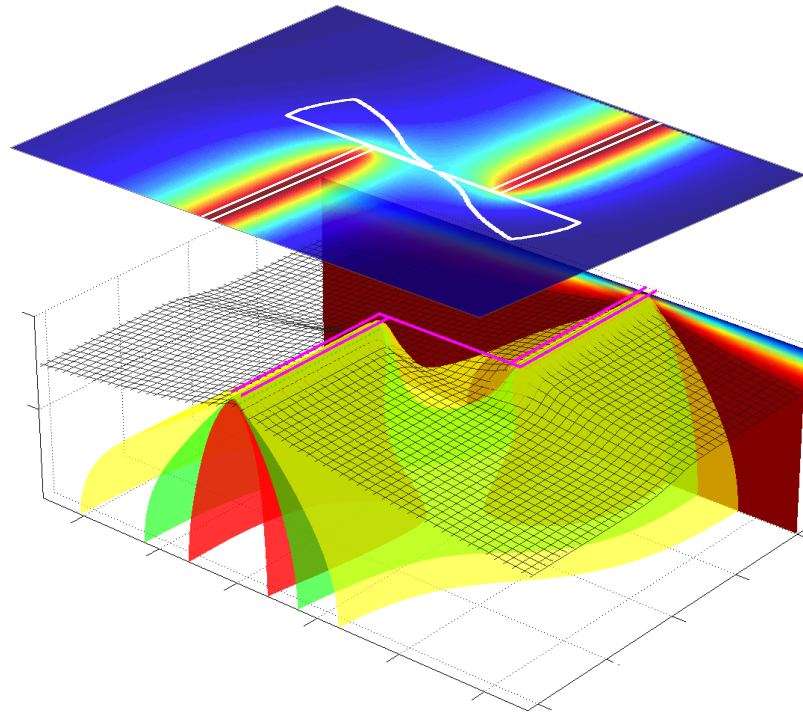


Influence of Mantle Dynamics on Global Patterns of Mid-Ocean Ridge Bathymetry



Samuel M Weatherley

University of Oxford

4th Year Master's Thesis

May 2009

Declaration

The project that follows has been written by, and is entirely the work of Samuel Weatherley.

Signed:

Date:

Word Count: 8113

Acknowledgements

Firstly I would like to thank my supervisor Richard Katz for devising what has been an interesting and rewarding Master's project, and for his continual support and encouragement. Lots of thanks are due to everyone in S4 for providing a welcoming and friendly working environment, for offering good support and advice and the opportunity to talk about elements of this project throughout the year.

I gratefully acknowledge the financial and computational support provided by the Oxford Supercomputing Centre. Special thanks are due to M. Duta and T. Sisiaridis for their help in overcoming technical difficulties early on in the project.

Finally, eternal thanks are due to Helen - thanks for everything.

Contents

Abstract

Global observations of mid-ocean ridge (MOR) bathymetry reveal a correlation between changes in the axial depth of MOR segments across ridge offsets and the direction of ridge migration. Segments leading with respect to the direction of ridge migration typically have a shallower bathymetry than the trailing segments. 2D numerical modelling of asthenospheric flow and melting predicts that ridge migration modifies the sub-ridge asthenospheric flow pattern. The modification of the flow pattern induces an asymmetry in melt production rates either side of the ridge axis. Analysis of the 2D model shows that differences in the focusing of melt from regions adjacent to ridge offsets can account for the observed variation in axial depth. However, the 2D model cannot properly simulate mantle dynamics and melting rate near ridge offsets. To better understand the dynamical interaction between plate tectonics and mantle convection, I have used a 3D numerical model to investigate the scale of asthenospheric flow and melting beneath migrating MOR. By coupling models of 3D melt focusing to my simulations, I generate predictions of axial depth changes across ridge offsets and of along axis variations in crustal thickness. Results of 3D simulations suggest that the behaviour of asthenospheric flow and melting is highly sensitive to the shape of the base of the lithosphere.

1 Introduction

At over 60,000 km long, the mid-ocean ridge (MOR) system is perhaps the most striking geological feature on Earth. Found only at constructive plate boundaries, MORs account for more than 60% by volume of the total annual flux of magma from the mantle to the crust. Magma generated at MORs is supplied to spreading segments that are offset by transform faults and smaller non-transform discontinuities. The morphology of ridge segments is thought to be controlled by variation in melt supply from the mantle. Although the variation in melt supply, and hence ridge segment morphology, has been attributed to the dynamics of sub-ridge mantle, the exact cause of the variation remains poorly under-

stood (??).

Global observations of MOR bathymetry reveal a correlation between differences in axial depth across ridge segment offsets and the direction of ridge migration in the hotspot reference frame (?). Segments leading with respect to the direction of ridge migration typically have a shallower bathymetry than the adjacent trailing segment (Figure ??). The ubiquity of this observation and its systematic connection with plate kinematics suggests an explanation might be related to plate induced mantle dynamics.

Kinematic models of plate driven mantle dynamics beneath MORs predict upwelling and melting to be symmetrical about non-migrating ridge segments, provided that both plates spread apart from the ridge at equal rates. In contrast, the same models predict significant asymmetry in upwelling and melting beneath a ridge migrating over the top of the asthenosphere. In the case of ridge migration, upwelling is more rapid and melting is greater beneath the leading plate (??).

Seismic and seafloor observations suggest that crustal formation occurs within a narrow zone (1-2 km) either side of the segment. To facilitate this, melts must be strongly focused to the ridge. In the case of a segmented spreading centre, focusing of melt can occur from the upwelling zone beneath the segment. Alternatively, melt may be focused from a region on the opposite side of the discontinuity to the ridge. These regions are denoted by Σ^+ and Σ^- for the leading and trailing segments respectively. This conceptual 3D melt focusing model is illustrated schematically in Figure (??).

In the absence of ridge migration melt would be focused from Σ^+ and Σ^- with equal efficiency because the melting rate is symmetrical about both ridge segments. If ridge migration occurs, the amount of melt focused from Σ^+ to the leading ridge segment is

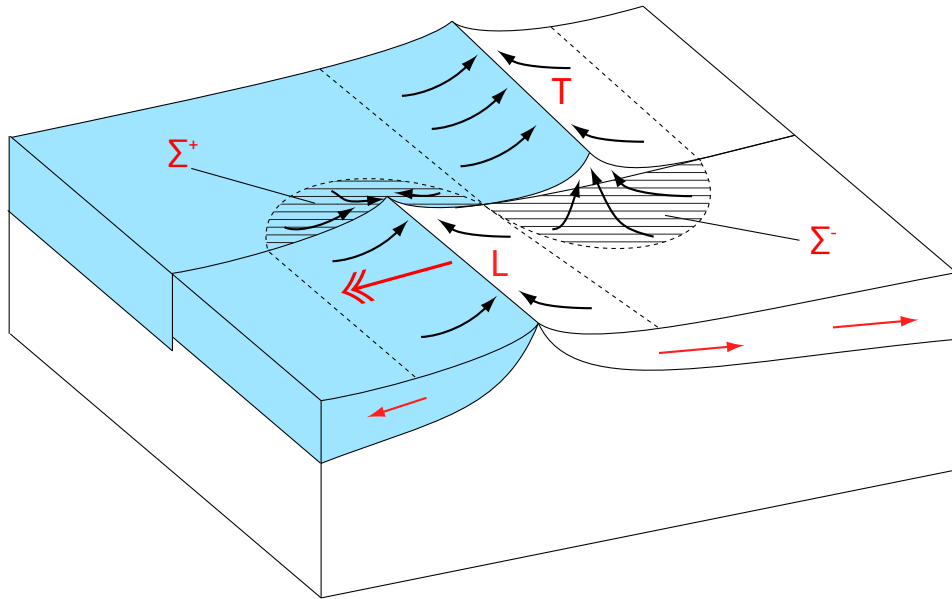


Figure 1: Schematic diagram showing a leading and trailing ridge segment separated by a discontinuity. Double headed red arrow indicates the direction of ridge migration. Single headed red arrows show the direction of lithosphere motion. The leading plate is coloured blue. L and T highlight the leading and trailing ridge segments respectively, which are surrounded by a focusing region (dashed lines). The focusing regions are divided into two sub-regions, one sub-region lies either side of the ridge axis and the other (hashed) lies on the opposite side of the discontinuity to the ridge. Hashed regions are labelled Σ^+ and Σ^- for the leading and trailing segments respectively. Black arrows depict hypothetical paths of melt focusing beneath the lithosphere. Modified from ?.

augmented and the amount of melt focused from Σ^- is diminished. This is caused by an asymmetry in melting rate about both ridge segments. Noting that all MORs are currently migrating relative to the hotspot reference frame (?), ? use this mechanism to explain the correlation between axial depth asymmetry and direction of ridge migration.

? quantify the conceptual model of ? with a 2D numerical model of asthenospheric flow and melting that considers non-Newtonian pressure (P), temperature (T) and strain

rate dependent mantle viscosity (η). They show that plate induced mantle dynamics is a plausible explanation for the observed morphological changes between MOR segments. Figures (??a,b) demonstrate that the 2D model predicts that mantle flow is symmetrical about the ridge axis in the absence of ridge migration, but asymmetrical about the axis when ridge migration occurs. Figure (??c) shows the component of mantle flow induced by ridge migration. This perturbed flow field is the difference between the mantle flow field in the case of ridge migration and the flow field in the case of no ridge migration.

In the absence of lithospheric plates, the perturbed flow would be simple shear with no component of vertical velocity. However, the curvature of the base of the lithosphere causes the perturbed flow to upwell under the leading plate and downwell beneath the trailing plate. By considering the melting rate to be a function of the vertical velocity [Section ??], the perturbed flow augments melt production beneath the leading plate and diminishes it beneath the trailing plate.

By coupling a simple parametric model of 3D melt focusing to the 2D model ? generate predictions of axial depth asymmetries across offsets between MOR segments. They define the focusing regions Σ^+ and Σ^- to be rectangular, of a size based on the characteristic distance (h) over which melt is focused to the ridge. Σ^+ and Σ^- extend h and $2h$ in the along and cross axis directions respectively. By fitting model results to observational data, ? estimate the focusing distance (h) to be 24 km. This contrasts with more recent work based on dynamical and thermodynamical calculations that suggest $h \sim 60$ km (?).

Constraints placed on the scale of melt focusing and upwelling geometry by the 2D model can be improved by computing 3D flow and temperature fields near ridge discontinuities. Several previous studies have addressed the three dimensional behaviour of mantle dynamics near ridge discontinuities. ? studied the development of multi-scale mantle flow

in a layered viscous mantle beneath mid-ocean ridge segments separated by a transform fault. Mantle flow beneath a triple junction in a mantle of variable viscosity was considered by ?. This finite element model also investigated the effects of differential motion of the triple junction with respect to the underlying mantle. Most recently, analytical solutions to plate driven flow in an incompressible, layered, viscous mantle beneath a generic ridge-transform-ridge plate boundary were calculated by ?.

In this thesis I use a numerical model to extend the study of ? into three dimensions. The model differs from those used in previous studies by employing the finite volume method to numerically solve for incompressible non-Newtonian plate driven mantle flow. With this model, I seek to determine whether lithosphere induced mantle dynamics can explain the global observations of variation in ridge bathymetry. By better understanding the scale of melt focusing and upwelling geometry, I aim to improve the constraints placed on these quantities by the 2D model of ?. The governing equations are discussed in Section ???. This is accompanied by an overview of the computational tools employed, the model setup and solution method. Melt focusing models are described in Section ??, followed by the results generated by the model (Section ??). The thesis is concluded with a discussion of the major findings.

2 Simulation of Mantle Dynamics

2.1 Governing Equations

A full description of physical dynamics in the sub-ridge mantle concerns the behaviour of the solid crystalline mantle and the liquid magma phase present within the solidus. In the limit of a rigid crystalline mantle, the governing equations reduce to Darcy's law for fluid flow in a porous medium. In the absence of a fluid phase, the equations reduce to a com-

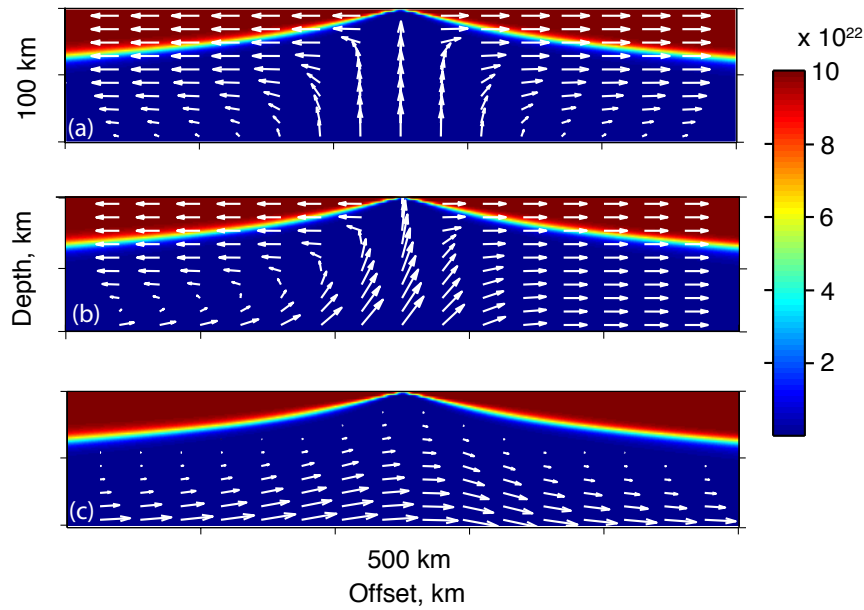


Figure 2: (a) Solid mantle flow pattern (white arrows) in the absence of ridge migration. Half spreading rate = 4 cm yr^{-1} . Background shows viscosity (Pa s^{-1}). (b) Pattern of solid mantle flow when rate of ridge migration = half spreading rate = 4 cm yr^{-1} . (c) Component of flow induced by ridge migration. This is calculated by subtracting the flow pattern in (a) from that in (b). Viscosity model employed is P , T and strain rate dependent.

plete description of solid mantle convection. ? provides a widely accepted formulation of the behaviour of two phase mantle flow by considering the conservation of mass, momentum and energy in the physical system. A numerical solution to such a set of equations is known here as a *simulation*. High computational cost prohibits large scale, high resolution simulations of two-phase mantle dynamics. The problem is made more tractable by solving the equations governing the dynamics of solid phase. By coupling a model of melting and melt migration to the simulation results, I significantly reduce to computational load and isolate important dynamical issues of the system.

The following set of coupled partial differential equations fully describe the dynamics of the solid phase:

$$\nabla \cdot \mathbf{v} = 0 \quad (1)$$

$$\nabla P = \nabla \cdot [\eta (\nabla \mathbf{v} + \nabla \mathbf{v}^T)] \quad (2)$$

$$\mathbf{v} \cdot \nabla \theta = \kappa \nabla^2 \theta. \quad (3)$$

Here, \mathbf{v} is the three dimensional velocity of the solid mantle, P is dynamic pressure, η is the mantle viscosity, κ is the thermal diffusivity and θ is the mantle potential temperature. Equation (2) stipulates that mass is conserved. Equation (3) governs the conservation of momentum of incompressible solid mantle in the limit of an infinitely small Reynolds number (Stoke's flow). Equation (3) is a statement of energy conservation and requires that, at a steady state, advection and diffusion of heat are in balance. A full derivation of these equations is given in Appendix 2.

Mantle deformation occurs through dislocation and diffusion creep. Diffusion creep is the dominant deformation mechanism at very low stress levels. When crystal grains are subjected to stress, atoms diffuse through the crystal interior. Consequently, crystal grains deform giving rise to rock strain. Newtonian fluids deform solely by diffusion creep. Dislocation creep can give rise to non-Newtonian fluid behaviour. Dislocations are imperfections in the crystal lattice structure. Examples of dislocation creep include the inclusion of extra planes of atoms in the lattice structure and out of plane deformation of the crystal lattice. Both of these dislocation types contribute to the development of stress within the crystal lattice. Stress development forces dislocations to propagate through the crystal lattices by slip and, when diffusion creep operates, climb. Fluids that deform by dislocation creep can behave in a non-Newtonian manner.

Dislocation creep creates a preferred orientation of minerals. Seismic studies of the sub-ridge asthenosphere (e.g., [1, 2, 3]) suggest preferred alignment of minerals can create a strong seismic anisotropy, thus demonstrating the importance of dislocation creep in the upper mantle. Dislocation creep is the dominant deformation mechanism in the upper mantle (4). Despite its importance, it is included in few numerical models. The viscosity (η)

is given by the harmonic mean of contributions from diffusion creep and dislocation creep.

$$\eta = \left(\frac{1}{\eta_{diffn}} + \frac{1}{\eta_{disl}} \right)^{-1} \quad (4)$$

where

$$\eta_{diffn} = A_{diffn} \exp \left(\frac{E_{diffn}^* + PV_{diffn}^*}{RT} \right) \quad (5)$$

$$\eta_{disl} = A_{disl} \exp \left(\frac{E_{disl}^* + PV_{disl}^*}{nRT} \right) \dot{\epsilon}_{II}^{(1-n)/n}. \quad (6)$$

A is a material parameter, E^* is activation energy, V^* is activation volume, R is the gas constant and n is the power law exponent (??, ??).

I aim to use the numerical model described in this thesis to isolate and investigate fundamental, global aspects of the mantle beneath migrating MORs, rather than simulate processes at specific geographical locations. For this reason, I prescribe simulations with realistic but hypothetical rates of ridge migration, half spreading rates and offsets. ?? showed that the mean ratio of the ridge-perpendicular migration rate (U_r) to half spreading rate (U_o) is 0.95 for medium and fast spreading ridges ($U_o > 3 \text{ cm yr}^{-1}$). For the purpose of these simulations, I use the approximation $U_r = U_o$.

2.2 Discretisation

The governing equations are discretised onto a staggered mesh using a finite volume approach (??) (Figure ??). In this method, the simulation domain is divided into uniform cells, or control volumes (Ω_{ijk}) where i , j , and k are the indices in the x , y and z directions respectively. x is aligned perpendicular to the ridge segments, y is aligned parallel to the ridge segments and z is aligned with the depth dimension. Temperature, pressure and viscosity are placed at the centre of each control volume, whilst the x , y and z com-

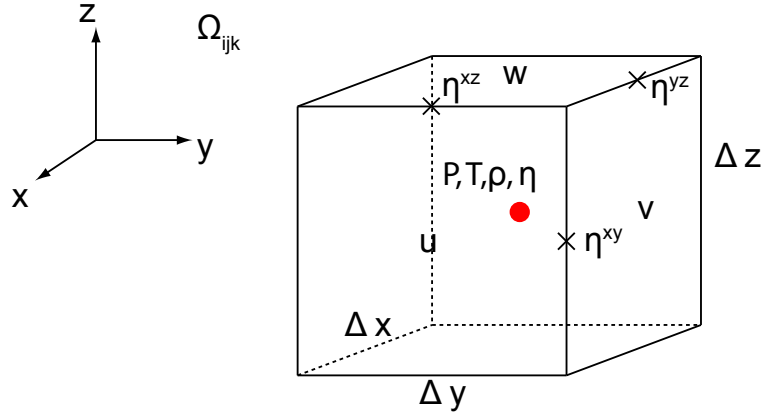


Figure 3: Control volume and staggered mesh. Each control volume has five degrees of freedom, u, v, w, P, T and their corresponding residuals.

ponents of the total velocity are located at the centre of cell faces normal to the direction of the velocity components. Spatial staggering of the velocity components allow the non-divergence of the flow field to be retained easily. The discretisation of the continuity equation (Equation ??) is shown below.

$$\frac{\int_V \nabla \cdot \mathbf{v} \, dV}{\int_V dV} = P_{ijk}^r$$

$$\frac{\int_{\partial V} \mathbf{v} \cdot \hat{\mathbf{n}} \, dS}{\int_V dV} = P_{ijk}^r$$

$$\frac{(u_{ijk} - u_{i-1jk}) \Delta y \Delta z + (v_{ijk} - v_{ij-1k}) \Delta x \Delta z + (w_{ijk} - w_{ijk-1}) \Delta x \Delta y}{\Delta x \Delta y \Delta z} = P_{ijk}^r$$

$$\frac{u_{ijk} - u_{i-1jk}}{\Delta x} + \frac{v_{ijk} - v_{ij-1k}}{\Delta y} + \frac{w_{ijk} - w_{ijk-1}}{\Delta z} = P_{ijk}^r \quad (7)$$

Here, u , v and w are the velocities in the x , y and z directions respectively. The cell dimensions are Δx , Δy and Δz . P_{ijk}^r is the residual of the continuity equation in cell Ω_{ijk} and corresponds to the pressure variable, despite the absence of a pressure term in the left hand side of Equation (??). u , v and w are obtained by discretising Equation (??).

Considering the x , y and z components separately

$$\begin{pmatrix} \frac{\partial P}{\partial x} \\ \frac{\partial P}{\partial y} \\ \frac{\partial P}{\partial z} \end{pmatrix} = \begin{pmatrix} \frac{\partial}{\partial x} \\ \frac{\partial}{\partial y} \\ \frac{\partial}{\partial z} \end{pmatrix} \cdot \left(\eta \left[\begin{pmatrix} \frac{\partial u}{\partial x} & \frac{\partial u}{\partial y} & \frac{\partial u}{\partial z} \\ \frac{\partial v}{\partial x} & \frac{\partial v}{\partial y} & \frac{\partial v}{\partial z} \\ \frac{\partial w}{\partial x} & \frac{\partial w}{\partial y} & \frac{\partial w}{\partial z} \end{pmatrix} + \begin{pmatrix} \frac{\partial u}{\partial x} & \frac{\partial v}{\partial x} & \frac{\partial w}{\partial x} \\ \frac{\partial u}{\partial y} & \frac{\partial v}{\partial y} & \frac{\partial w}{\partial y} \\ \frac{\partial u}{\partial z} & \frac{\partial v}{\partial z} & \frac{\partial w}{\partial z} \end{pmatrix} \right] \right). \quad (8)$$

$$-\frac{P_{i+1jk} - P_{ijk}}{\Delta x} + \frac{\sigma_{i+1jk}^{xx} - \sigma_{ijk}^{xx}}{\Delta x} + \frac{\sigma_{ijk}^{xy} - \sigma_{ij-1k}^{xy}}{\Delta y} + \frac{\sigma_{ijk}^{xz} - \sigma_{ijk-1}^{xz}}{\Delta z} = u_{ijk}^r \quad (9)$$

$$-\frac{P_{ij+1k} - P_{ijk}}{\Delta y} + \frac{\sigma_{ijk}^{xy} - \sigma_{ij-1k}^{xy}}{\Delta x} + \frac{\sigma_{ij+1k}^{yy} - \sigma_{ijk}^{yy}}{\Delta y} + \frac{\sigma_{ijk}^{yz} - \sigma_{ijk-1}^{yz}}{\Delta z} = v_{ijk}^r \quad (10)$$

$$-\frac{P_{ijk+1} - P_{ijk}}{\Delta z} + \frac{\sigma_{ijk}^{xz} - \sigma_{i-1jk}^{xz}}{\Delta x} + \frac{\sigma_{ijk}^{yz} - \sigma_{ij-1k}^{yz}}{\Delta y} + \frac{\sigma_{ijk+1}^{zz} - \sigma_{ijk}^{zz}}{\Delta z} = w_{ijk}^r \quad (11)$$

where

$$\sigma_{ijk}^{xx} = 2\eta_{ijk} \frac{u_{ijk} - u_{i-1jk}}{\Delta x} \quad (12)$$

$$\sigma_{ijk}^{yy} = 2\eta_{ijk} \frac{v_{ijk} - v_{ij-1k}}{\Delta y} \quad (13)$$

$$\sigma_{ijk}^{zz} = 2\eta_{ijk} \frac{w_{ijk} - w_{ijk-1}}{\Delta z} \quad (14)$$

$$\sigma_{ijk}^{xy} = \eta_{ijk}^{xy} \left(\frac{u_{ij+1k} - u_{ijk}}{\Delta y} + \frac{v_{i+1jk} - v_{ijk}}{\Delta x} \right) \quad (15)$$

$$\sigma_{ijk}^{xz} = \eta_{ijk}^{xz} \left(\frac{u_{ijk+1} - u_{ijk}}{\Delta z} + \frac{w_{i+1jk} - w_{ijk}}{\Delta x} \right) \quad (16)$$

$$\sigma_{ijk}^{yz} = \eta_{ijk}^{yz} \left(\frac{v_{ijk+1} - v_{ijk}}{\Delta z} + \frac{w_{ij+1k} - w_{ijk}}{\Delta y} \right). \quad (17)$$

For each control volume, u_{ijk}^r , v_{ijk}^r and w_{ijk}^r are the u , v and w velocity residuals in cell Ω_{ijk} respectively and σ is stress. Linear interpolation has been used to define the viscosities η_{ijk}^{xy} , η_{ijk}^{xz} and η_{ijk}^{yz} on the control volume's edges (Figure ??). The discretisation is

discussed more fully in ?. To more properly simulate advection and diffusion of heat, an upwind scheme is employed in which the stencil is biased in the direction of heat transport. ? discretises the advection term in Equation (??) using the Fromm scheme described by ?. Central differencing techniques are employed to discretise the diffusion term.

2.3 Boundary Conditions

The governing equations are solved in a reference frame fixed to the migrating ridge. To solve Equations (?? - ??), physically motivated boundary conditions must be specified on u , v , w , P and T . The complete set of boundary conditions is given in Table (1). On the top boundary (corresponding to the top of the lithosphere), T is set to zero and u , v , w are set such that they describe the plate motion. The bottom boundary corresponds to the bottom of the asthenosphere. The dimensionless T is set equal to the dimensionless θ , and w is set so that there is constant inflow of solid mantle. Because the governing equations are solved in a reference frame fixed to the migrating ridge, the horizontal velocity is set equal to the ridge migration rate U_r . Since the boundaries perpendicular to the ridge segments are not physical, frictional boundaries, the flow is prescribed to slip smoothly along them. The fact that a staggered mesh is used sometimes results in a boundary condition having no influence on the interior of the domain.

2.4 Computational Tools

The zone of melting beneath a mid-ocean ridge may extend laterally for hundreds of kilometres under each plate and down to depths in excess of 60 kilometres. A successful study of sub-ridge asthenospheric flow requires 3D simulations to be run in a large physical domain at high resolution. In such a large domain, solutions to the governing system of coupled differential equations exceeds the capabilities of general-purpose high-level languages such as MATLAB and desktop computers. Multiprocessor (parallel) computing

Table 1: Boundary Conditions

Boundary	Variable	Boundary condition	Physical significance
$z = 0$	u	$u(x, y, 0) = U(x, y)$	U is the prescribed plate motion
	v	$v = 0$	Plate does not move in the y -direction
	w	$w = 0$	Impermeability
P		BC does not influence the interior of the domain	
	T	$T = 0$	
$z = Z$	u	$u = U_r$	U_r is the x -component of ridge migration V_r is the y -component of ridge migration Constant inflow
	v	$v = V_r$	
	w	$\partial w / \partial z = 0$	
	P	$P = 0$	
T		1	Dimensionless T set equal to θ (dimensionless)
$x = 0, X$	u	Satisfies Equation (??)	Flow is normal to domain boundary
	v	$v = 0$	
	w	$w = 0$	
P		BC does not influence the interior of the domain	
T		$\partial T / \partial x = 0$	
$y = 0, Y$	u	No stress: $\eta (\partial u / \partial y + \partial v / \partial x) = 0$	Flow slips smoothly along y boundary since it does not represent a physical, frictional boundary.
	v	No stress: $2\eta \partial v / \partial y - P = 0$	
	w	No stress: $\eta (\partial v \partial z + \partial w / \partial z) = 0$	
	P	BC does not influence the interior of the domain	
T		$\partial T / \partial y = 0$	

The domain size is $x \in [0, X]$, $y \in [0, Y]$, $z \in [0, Z]$. The x dimension is parallel to the spreading rate vector and transform faults, and the spreading ridge is parallel to the y dimension.

systems are needed to handle these large simulations. The governing equations are solved by a program written in C that implements the Portable, Extensional Toolkit for Scientific Computing (PETSc). PETSc is an advanced numerical software library that contains a range of inherently parallel data structures, preconditioners and solvers with a constant user interface to ease the development and running of complex parallel simulations.

Simulation success depends heavily on effective communication between different processors. Communication has been facilitated through the development of the Message Passing Interface (MPI), which provides a standard means of efficient inter-processor communication for parallel computers. For successful implementation of MPI, every aspect of parallelism and processes must be managed by the programmer. PETSc aims to remove direct use of MPI, leaving the programmer to focus on the overall computation and detailed physics of the simulation. Parallelisation provides an additional challenge in reaching a numerical solution with successful implementation of the boundary conditions. Inter-processor communication is needed so that all processes contribute to a solution that satisfies the boundary conditions. Inter-processor communication is facilitated through the use of ghost points (Figure ??) - an additional line of cells surrounding cells on a processor that contain information about the neighbouring processes.

Solution method

By assembling the complete set of degrees of freedom into a vector \tilde{x} of length $N = 5N_c$ where N_c is the total number of grid cells, the nonlinear set of discretised equations can be represented as

$$\mathbf{A}(\tilde{x}) = 0. \quad (18)$$

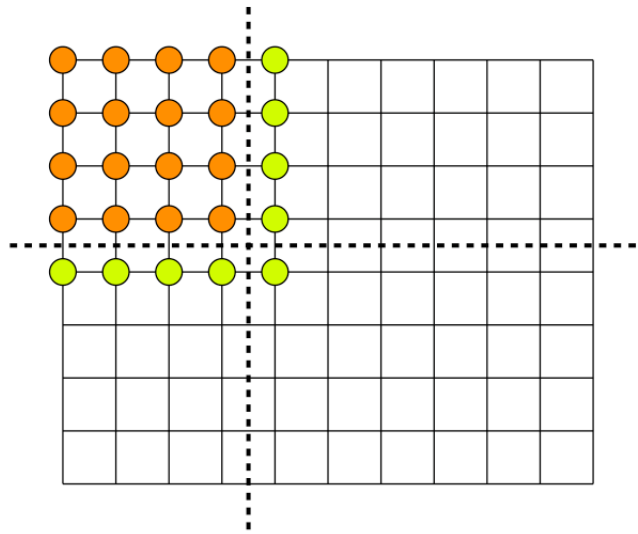


Figure 4: Ghost point principles. The black dashed lines show how the mesh is divided between the different processors. Orange points represent the portion of the mesh held on one of the processors. The green points represent ghost points. These ghost points are held on the same processor as the orange points, but contain information about the neighbouring processes to ensure continuity of the solution across processors.

In practice it is difficult to find a vector \tilde{x} such that $\mathbf{A}(\tilde{x})$ is exactly equal to a zero vector. Instead, an approximate solution is iterated to such that

$$\|\mathbf{A}(\tilde{x})\| = \|\tilde{r}\| < tol \quad (19)$$

where $\|\cdot\|$ is the vector norm, \tilde{r} is a vector of length N containing the residuals of $\mathbf{A}(\tilde{x})$ and tol is a tolerance of the order 10^{-4} . The isoviscous case is linear and can be solved analytically by direct inversion. However, models with variable viscosity require use of an iterative method. For example

for $n = 1, 2, \dots$

$$\tilde{r}^n = \mathbf{A}(\tilde{x}^n)$$

$$\tilde{x}^{n+1} = \tilde{x}^n + f(\tilde{r}^n).$$

where n represents the iteration. Given a good starting guess \tilde{x}^* to the solution \tilde{x}_0 , the Newton-Raphson method provides one way with which a solution can be obtained. If \tilde{x}^* differs from the solution to \tilde{x}_0 by an amount $\delta\tilde{x}$, i.e.

$$\tilde{x}^* = \tilde{x}_0 + \delta\tilde{x}$$

$\mathbf{A}(\tilde{x}^*)$ can be expanded in a Taylor series about \tilde{x}_0

$$\mathbf{A}(\tilde{x}^*) = \mathbf{A}(\tilde{x}_0 + \delta\tilde{x}) = \mathbf{A}(\tilde{x}_0) + \delta\tilde{x} \cdot \nabla[\mathbf{A}(\tilde{x}_0)] + \dots \quad (20)$$

Equation (??) is then reduced and solved linearly to obtain $\delta\tilde{x}$

$$\delta\tilde{x} \approx \mathbf{A}(\tilde{x}^*) \cdot [\nabla\mathbf{A}(\tilde{x}_0)]^{-1}. \quad (21)$$

This is implemented by the iterative method as shown below:

for $n = 1, 2, \dots \{$

/ Evaluate residual */*

$$\tilde{r}^n = \mathbf{A}(\tilde{x}^n)$$

if $n = 2, 3, \dots \{$

*/*Check for convergence */*

$$\tilde{r}^n < \tilde{r}^{n-1}$$

$\}$

/ Compute Jacobian */*

$$J_{ij}^n = \frac{\partial r_i^n}{\partial x_j^n}$$

/ Linear solve for $\delta\tilde{x}$ */*

$$J^n \delta \tilde{x} = \tilde{r}^n$$

/ Correct starting guess */*

$$\tilde{x}^{n+1} = \tilde{x}^n - \delta \tilde{x}$$

}

This process is repeated until $\|\tilde{r}\| < tol$. The highly nonlinear dependence of viscosity on T , P and strain rate prevents Newton's method converging to a solution unless a good starting guess is used. To convergence and provide a good initial guess, a continuation method is adopted. In this method the viscosity is raised to a power between zero and one, $\eta \rightarrow \eta^\alpha$ (?). $\alpha = 0$ corresponds to constant viscosity and $\alpha = 1$ corresponds to the full variation in viscosity. In this way the variation in viscosity is forced to go from zero to the full variation over a set of iterations of the nonlinear solve.

3 Melting and Melt Migration

This study concerns the scale and distribution of upwelling and melting in the sub-ridge asthenosphere. Computational constraints preclude calculation of compressible two-phase flow and thermodynamically governed melting in large scale three dimensional calculations. Therefore I assume that Equations (??-??) isolate the important aspects of upwelling and melting behaviour. Solutions to the governing equations are processed with a simple melting model stating that the melting rate (Γ) in cell Ω_{ijk} is given by

$$\Gamma_{ijk} = \rho_m W_{ijk} \left. \frac{dF}{dz} \right|_S \quad (22)$$

where W is vertical velocity, dF/dz is the adiabatic productivity and S is entropy. In a parameterisation study of mantle melting, ? show that the melting rate for a mantle potential temperature of 1300°C is approximately constant at $0.2\% \text{km}^{-1}$. As a consequence,

Γ is a function of W only. The melting region is defined as the zone in which T is greater than the temperature of the solidus ($T_{solidus}$) and $|W| > 0$. The change in $T_{solidus}$ with depth caused by adiabatic decompression is given by $T_{solidus} = A_1 + A_2P - A_3P^2$ where $A_1 = 1085.7^\circ\text{C}$, $A_2 = 132.9^\circ\text{C GPa}^{-1}$ and $A_3 = -5.1^\circ\text{C GPa}^{-2}$.

The intricacies of the melt focusing process are poorly understood. ? model magma migration as porous flow in which viscous interaction between the melt and solid matrix resists magma flow. They show that the velocity of the solid mantle is at least two orders of magnitude less than the magma migration velocity, suggesting that advection of melt by the porous solid mantle is negligible. ? use this assumption in a model of melt focusing. They describe how a balance of compaction and viscous forces dilates the porous mantle at the top of the melting region to form a high porosity channel. The channel is overlain by impermeable mantle. Melt upwells buoyantly to the channel where it is driven towards a ridge segment by the along channel component of gravity.

Based on the model of ? I have developed an algorithm to calculate the effect of 3D melt focusing for each simulation. The algorithm (code provided in Appendix ??), assumes that melt upwells buoyantly to a high porosity channel coincident with the upper surface of the melting region. Melts migrate along streamlines (\tilde{s}) that are tangential to the steepest local slope of the upper surface of the melting region, i.e.

$$\tilde{v} \times d\tilde{s} = 0 \quad (23)$$

where

$$\tilde{v} = \frac{\partial \mathbf{m}}{\partial x} + \frac{\partial \mathbf{m}}{\partial y}. \quad (24)$$

Here \mathbf{m} is the depth to the upper surface of the melting region and \tilde{v} is the steepest local slope of this surface. Streamlines are calculated for each grid cell in \mathbf{m} within one

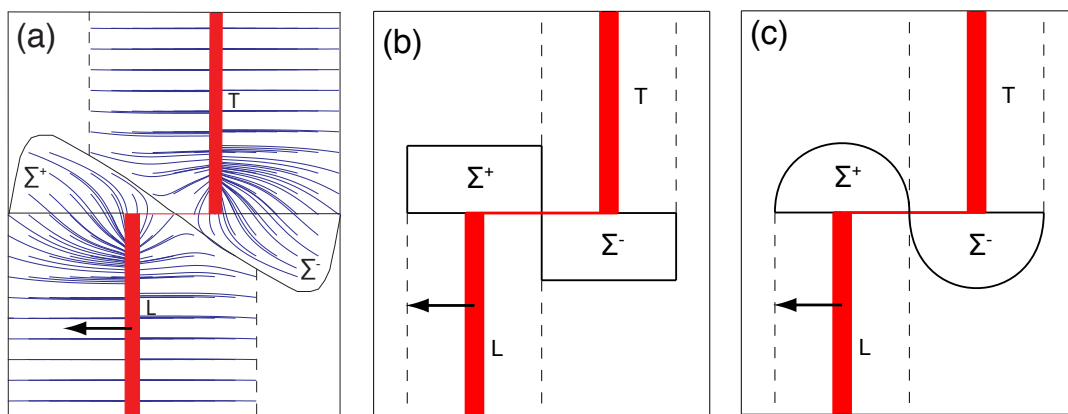


Figure 5: Schematic diagrams showing the principles of the different focusing algorithms. Red bars and lines show the positions of the ridge segments and transform faults. Black solid lines outline Σ^+ and Σ^- and black dashed lines show the along-axis region from which melt is drawn. L: leading ridge segment, T: trailing ridge segment. Black arrow shows direction of ridge migration. (a): streamline focusing algorithm. Blue streamlines show the path melt takes as it is focused to the ridge. Here the focusing distance (h) is greater than the offset but the topography of the melting region prevents Σ^+ and Σ^- from overlapping. (b): Rectangular focusing algorithm. The focusing distance, h is equal to half of the offset. No overlap between Σ^+ and Σ^- occurs. (c) Nearest focusing algorithm. Again, h is half of the offset length.

focusing distance h of all ridge segments. If a streamline crosses into a narrow (1 km) zone around each ridge segment, all melt present at the starting point of the streamline is focused to the ridge segment. Hence, this narrow zone is termed the *crustal generation region*. ? notes that the efficiency of melt extraction is greater than 70%. For the purpose of this investigation, which concerns the scale of asthenospheric flow and melting, it is reasonable to assume complete extraction of melt from the mantle with the focusing regions. Assuming there is no redistribution of melt within the crustal generation region, this algorithm calculates (i) the difference in amount of melt delivered from Σ^+ and Σ^- and (ii) the along axis variation of crustal thickness. This algorithm is known as the Streamline focusing algorithm and is illustrated schematically in Figure (??).

3D simulations are approximately 25000 times more computationally expensive than analogous 2D simulations. It would be advantageous to more accurately simulate the

effects of 3D melt focusing using the 2D model. Two further algorithms were developed to test simple geometrical models of 3D melt focusing against the Streamline focusing algorithm. Both models are similar to that used in ?. The algorithms only assess the difference in amount of melt focused to the ridge from Σ^+ and Σ^- . The first algorithm involves integrating Γ first over depth to give the *vertically integrated melting rate* Γ_I (i.e. $\Gamma_I = \int_0^Z \Gamma dz$) and then over Σ^+ and Σ^- . The regions Σ^+ and Σ^- have dimensions $2h$ and h in the cross and along axis directions respectively. This method is comparable to the simple 3D focusing model used by ? and is known as the Rectangular focusing algorithm.

The second method instead approximates the shape of the focusing region to be a half-circle with radius h , as shown in Figure (??) and is known as the Half-Circle focusing algorithm. The Rectangular and Half-Circle focusing algorithms assume all melt within Σ^+ is focused to the leading ridge segment, and all melt within Σ^- is focused to the trailing segment. However, similar to the focusing model used by ?, the physical feasibility of the algorithms breaks down at offset lengths less than h because Σ^+ and Σ^- are allowed to overlap on to the adjacent ridge segments.

4 Results

Figure (??) shows that ridge migration produces asymmetry in the 3D melting rate simulations. The peak Γ_I occurs at the ridge axis, immediately under which $|W|$ peaks at all depths. The highest upwelling rates are of similar magnitude to the half spreading rate. Without ridge migration, $|W|$ and $|\Gamma_I|$ decay away symmetrically either side of the ridge. When $U_r = U_0$, the distance over which $|W|$ and $|\Gamma_I|$ decay to zero increases with spreading rate. However, $|W|$ and $|\Gamma_I|$ decay more slowly on the leading side of the ridge causing simulations to show a pronounced cross axis asymmetry. Comparing the amount of melt generated on the leading side to the trailing side gives a measure of asymmetry.

Asymmetry varies from 16% when $U_r = U_o = 1 \text{ cm yr}^{-1}$, offset = 10 km to 38% when $U_r = U_o = 6 \text{ cm yr}^{-1}$, offset = 80 km.

Figure (??) shows that the focusing sub-regions Σ^+ and Σ^- can be considered in 3D and 2D. In 3D, Σ^+ and Σ^- would be volumes, bounded on their upper and lower surfaces by the melting region and controlled laterally by the shape of the melting region and the prescribed focusing distance. However, Figure (??b) shows a more simple 2D representation of the focusing sub-regions. The outline of Σ^+ and Σ^- is defined by the zone on the upper surface of the melting region from which melt is focused to the ridge segment.

4.1 Morphological Asymmetry

Figure (??) shows how the morphological asymmetry (the difference in axial depth across an offset) predicted by 2D and 3D simulations varies as a function of offset. Assuming that melt focused from Σ^+ and Σ^- is distributed evenly over the first 1 km of the ridge segments, the curves in Figure (??) are obtained using

$$\Delta H = \frac{\int_{\Sigma^+} \Gamma_1 dA - \int_{\Sigma^-} \Gamma_1 dA}{2 \rho_c U_o} \quad (25)$$

where

$$\Gamma_1 = \int_0^Z \Gamma dz \quad (26)$$

Here, Γ is the melting rate ($\text{kg m}^{-3} \text{ yr}^{-1}$), Γ_1 is the vertically integrated melting rate ($\text{kg m}^{-2} \text{ yr}^{-1}$), ρ_c is the density of the oceanic crust. Assuming ridge topography is approximately isostatically balanced and a crustal density of 2900 kg m^{-3} , the topographic asymmetry $\Delta d = 0.17 \Delta H$ (?).

Result from 3D simulations presented in Figure (??) have been obtained using a focusing

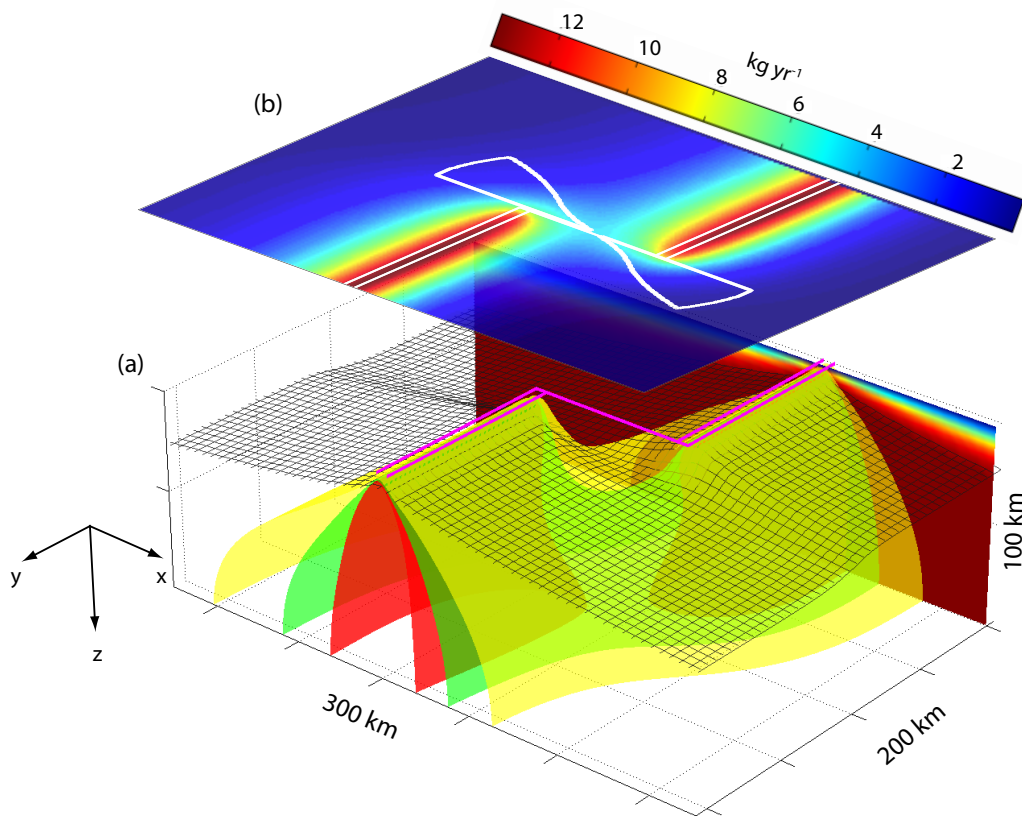


Figure 6: Example output from a 3D simulation with $U_r = U_o = 4 \text{ cm yr}^{-1}$. Offset = 80 km. (a) shows a 3D image of the upwelling geometry beneath the ridge system denoted by magenta lines. The ridge is migrating to the left. Red, green and yellow surfaces show constant upwelling rates of 1, 2 and 2.75 cm yr^{-1} respectively. Upwelling is strongly asymmetrical about the ridge axis. Wire mesh marks the base of the lithosphere, defined by the locus of the maximum rate of change in viscosity in the z -direction. Back wall shows a 2D slice taken across the trailing segment through the temperature field. Dark red represents the mantle potential temperature (1300°C) and dark blue indicates 0°C . (b) Map of the vertically integrated melting rate, Γ_I (i.e. $\Gamma_I = \int_0^Z \Gamma dz$). White lines show location of the ridge segments, transform fault, Σ^+ (furthest left) and Σ^- (furthest right). The vertically integrated melting rate shows the amount of melt beneath any point on the surface of the solidus that can be focused to a ridge segment.

distance (h) of 55 km, whilst 2D simulations have been processed with $h = 24$ km. ? use $h = 24$ km and asthenospheric depth of 670 km to achieve a best fit between 2D model results and observational data, although the amplitude of their results scales inversely with asthenospheric depth. The asthenospheric depth is restricted to 100 km, because large scale, high resolution simulations with domain depths in excess of 100 km become too computationally expensive. Assuming that the inverse scaling relationship observed by ?

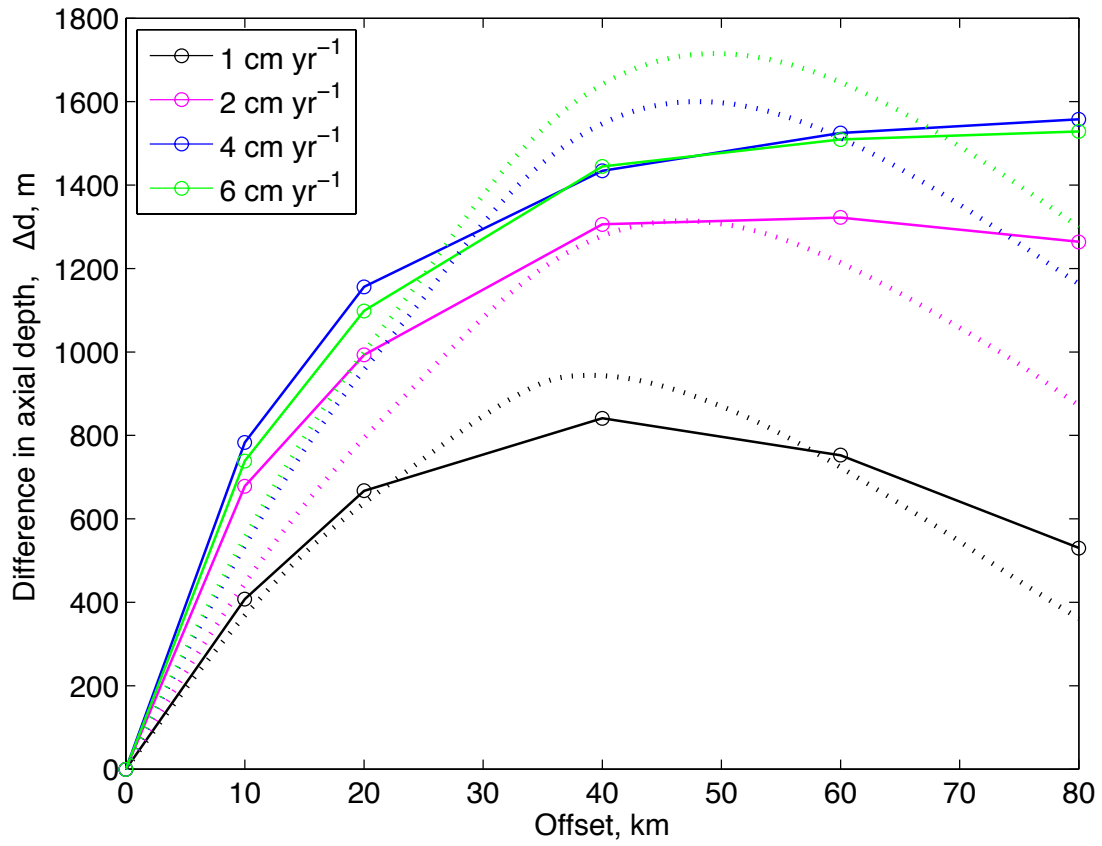


Figure 7: Simulation results of asymmetry as a function of offset. Curves show the predicted difference in axial depth Δd as a function of offset for a range of spreading rates and offsets. Solid curves show results of 3D simulations, and dotted curves show results from analogous 2D simulations. Each open circle represents one 3D simulation. 3D simulations have been processed using the Streamline focusing algorithm and a focusing distance of 55 km. 2D simulations are processed using a focusing distance of 24 km, which ? use to achieve a best 'by-eye' fit between their simulation output and real data. The grid resolution is 3 km. The asthenospheric depth for all simulations is set to 99 km.

remains pertinent to the 3D case, h is estimated for the 3D model by comparing morphological asymmetry curves from analogous 2D and 3D simulations. 3D simulation results best fit 2D results (use $h = 24$ km) when $h = 55$ km.

The 2D and 3D results shown in Figure (??) show broadly similar trends. However, it is clear that significant differences exist between the 2D and 3D system. 2D simulations predict an increase in morphological asymmetry (Δd) with offset from zero to

a peak value. The peak value increases slightly with spreading rate from 40 km when $U_r = U_0 = 1 \text{ cm yr}^{-1}$ to 50 km when $U_r = U_0 = 6 \text{ cm yr}^{-1}$. After the peak value has been reached, Δd decreases with further increase in offset such that the curves in Figure (??) are asymmetrical about their peak. Δd increases with spreading rate (at decreasing rate) at all offsets.

When $U_r = U_0 = 1$ and 2 cm yr^{-1} , 3D simulations predict that morphological asymmetry (Δd) increases with offset up to a peak value. In these cases, Δd decreases with further increase in offset after the peak value has been reached. The curves for simulations with $U_r = U_0 = 1$ and 2 cm yr^{-1} are asymmetrical about their peak. Simulations for $U_r = U_0 = 4 \text{ cm yr}^{-1}$ and $U_r = U_0 = 6 \text{ cm yr}^{-1}$ do not show a peak value. Instead they show an increase in morphological asymmetry with offset with asymmetry for all cases simulated, although the slope of the results decreases as offset increases. In contrast to the results from 2D simulations, the values of morphological asymmetry for 3D simulations with $U_r = U_0 = 4 \text{ cm yr}^{-1}$ and $U_r = U_0 = 6 \text{ cm yr}^{-1}$ show a close fit.

Figure (??) shows the relative behaviour of the different melt focusing algorithms when $h = 55 \text{ km}$. Results generated by the 2D model using $h = 24 \text{ km}$ have been included for comparison. The focusing distance used to process the 2D results has been obtained by fitting model results to observed data. Recent dynamical and thermodynamical calculations (?) suggest that $h \sim 60 \text{ km}$. This closely agrees with the focusing distance of 55 km that best fits 3D simulation results to reference results generated by the 2D model. Of the three focusing algorithms used to process results from 3D simulations, results returned by the Streamline algorithm fit closest to the 2D predictions of morphological asymmetry. At all offsets, the morphological asymmetries predicted by the Rectangular and Half-Circle algorithms are more than double those predicted by the Streamline algorithm. These results do not share a close fit with the 2D reference results. Owing to this fact, the Streamline algorithm offers a better simulation of 3D melt focusing than the Rectangular or Half-

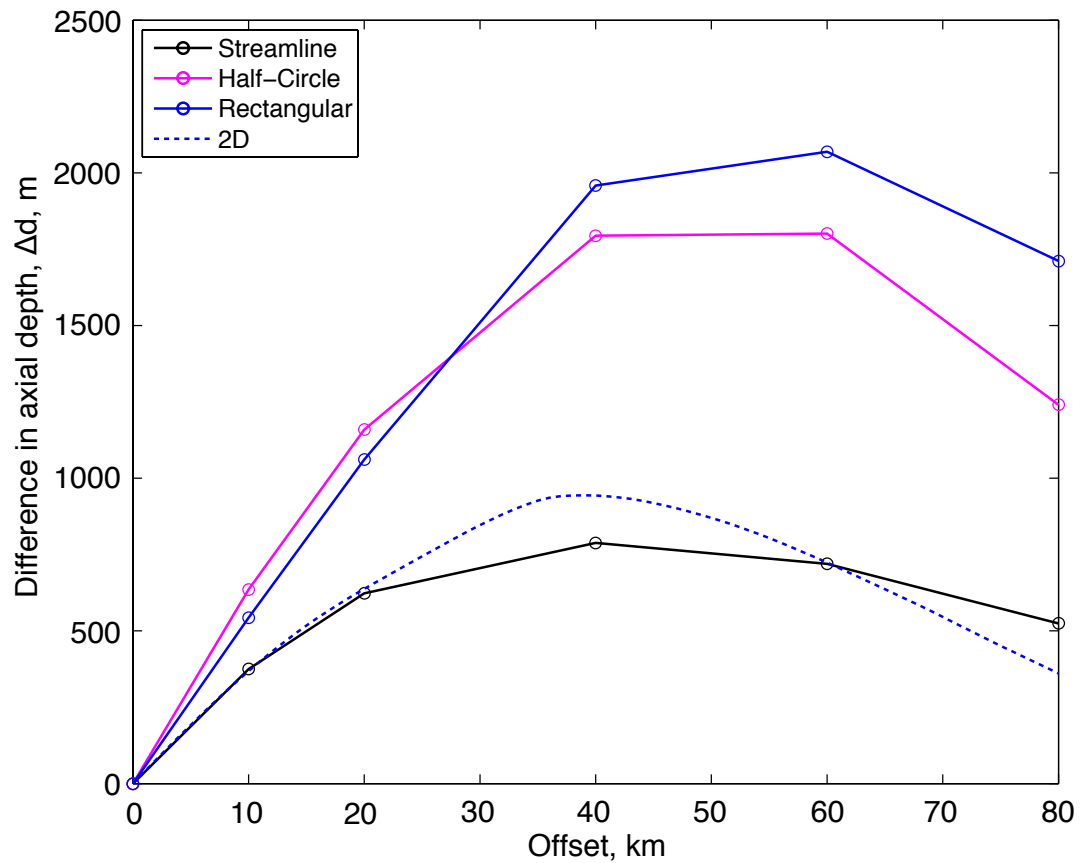


Figure 8: Comparison of the behaviour of the different focusing algorithms. 3D simulations have $U_r = U_0 = 1 \text{ cm yr}^{-1}$. Domain depth is 99 km. The focusing distance (h) is 55 km for all 3D results presented here. 2D curve is produced from a completely analogous simulation, but is processed using $h = 24 \text{ km}$.

Circle methods.

4.2 Variation in Crustal Thickness

Figure (??) shows profiles of crustal thickness predicted by analysing 3D simulation results with the Streamline algorithm. All profiles show a region of very thin crust close to the transform fault. With increasing distance from the transform fault in the along axis direction, the crustal thickness peaks before decaying to a constant thickness. The distance between the transform fault and peak crustal thickness decreases with increasing spreading rate. Similarly, the crustal thickness at large distances from the transform fault scales inversely with spreading rate. Again, as in Figure (??), results from simulations with $U_r = U_0 = 4 \text{ cm yr}^{-1}$ and $U_r = U_0 = 6 \text{ cm yr}^{-1}$ share a close fit.

The Streamline algorithm predicts the average crustal thickness to be 3.4 km. However, the real oceanic crust has an average thickness of $7 \pm 1 \text{ km}$. Further discrepancies exist between the predicted crustal thickness (Figure ??) and real data. ? show that the thickness of the oceanic crust does not vary with spreading rate and full spreading rates greater than 3 cm yr^{-1} . When the full spreading rate is less than 3 cm yr^{-1} , conduction of heat from the melting region causes crustal thickness to decrease with decreasing spreading rate. ? note that the oceanic crust thins towards transform faults, as shown in Figure (??). However, observational data suggest that the oceanic crust only thins to approximately 4 km, not $< 1 \text{ km}$ as predicted.

5 Geometry and Scale of Melting and Upwelling

The simulation results can be understood by considering the component of mantle flow induced by ridge migration. Figure (??c) shows that the curvature of the base of the

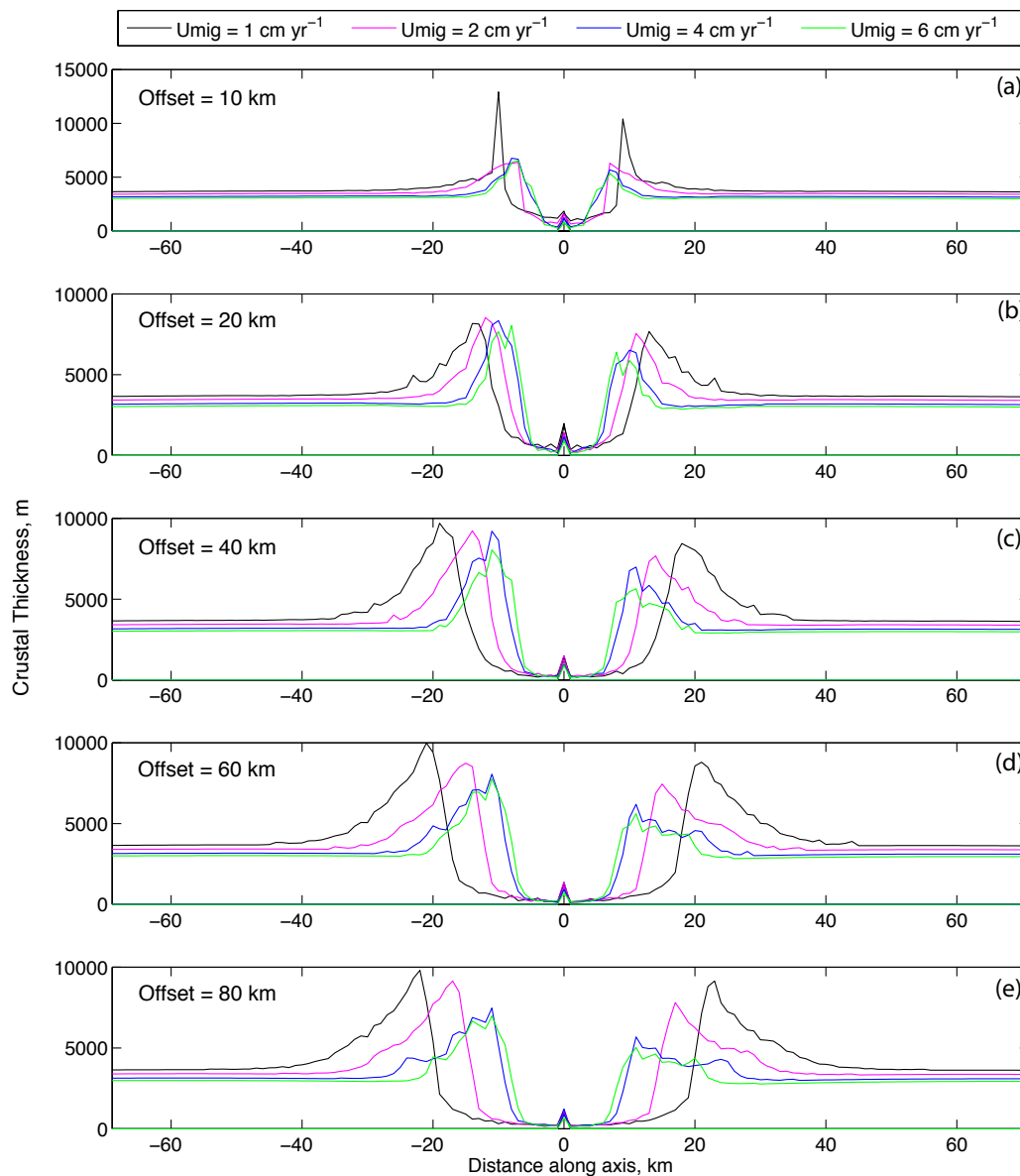


Figure 9: Profiles of along axis crustal thickness generated by the Streamline algorithm. Profiles for the leading ridge segment are plotted on the left of each panel (distance along axis < 0 km). All crustal thickness profiles have been stacked into the same plane.

lithosphere causes the perturbed flow to upwell beneath the leading plate and downwell beneath the trailing plate. In this thesis I define the base of the lithosphere to be where the rate of change of viscosity with depth reaches a maximum. The perturbed flow causes all asymmetry in melting rate and, hence, axial depth.

5.1 Peak Morphological Asymmetry

All 2D and some 3D simulation results presented in Figure (??) show that the morphological asymmetry will peak at some offset. Equation (??) shows that the vertical component of velocity of the perturbed flow (W') induces a perturbation in the melting rate (Γ'), i.e. $\Gamma' \propto W'$. The offset at which the difference in Γ' between the regions Σ^+ and Σ^- is maximum corresponds to the position of peak morphological asymmetry.

Figure (??a) shows surfaces of maximum $|W'|$ at all depths greater than 20 km. The surfaces of maximum $|W'|$ are known as the *extremal surfaces*. Owing to Equation (??), the location of maximum Γ' corresponds to the position of the extremal surfaces within the melting region. The maximum difference in perturbed melting rate (Γ'), and hence peak morphological asymmetry (Figure ??) occurs when the extremal surfaces bisect Σ^+ and Σ^- .

To illustrate this, Figure (??b) shows W' interpolated on to the base of the melting region. The simulation used to plot Figure (??b) generates peak morphological asymmetry ($U_r = U_0 = 1 \text{ cm yr}^{-1}$, offset = 40 km). On this surface $|W'|$ and $|\Gamma'|$ reach their maximum values within the melting region. The trace of these maximum values can be seen to bisect the regions Σ^+ and Σ^- .

5.2 Asymmetry Generated Far From Transform Faults

Figure (??) shows that the difference in axial depth between leading and trailing ridge segments increases with spreading rate when $U_r = U_0$. This is best understood by considering the effect of the lithosphere on mantle flow far from the transform fault because the shape of the base of the lithosphere varies only in the cross axis direction. ? describe how

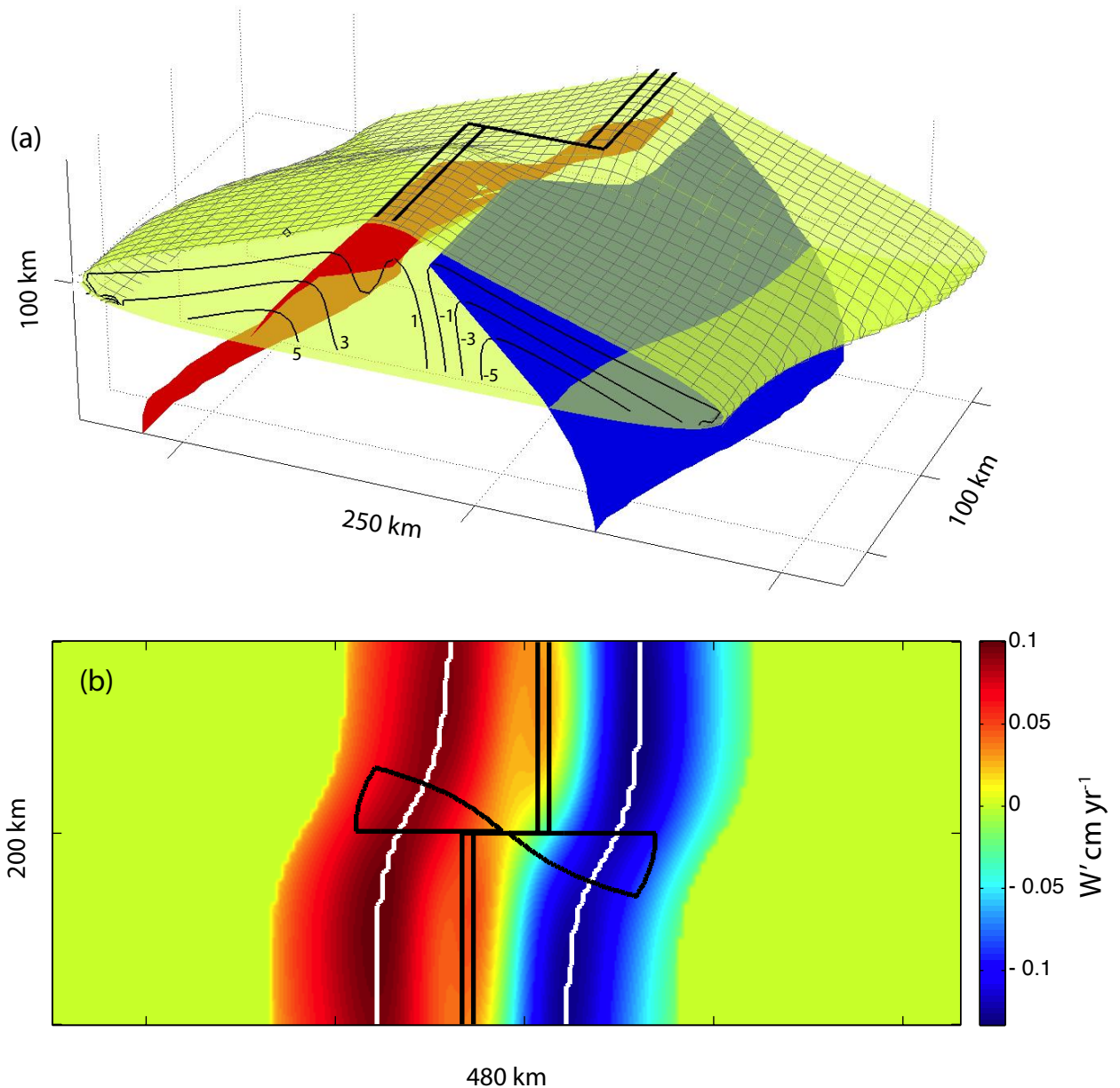


Figure 10: (a) Figure shows melting region (green surface with grey wire mesh) and extremal surfaces of W' . Red extremal surface shows W'_{max} , blue surface shows W'_{min} . Black contours denote $|\Gamma'|$ of 1, 3 and 5 $\text{kg m}^{-3} \text{yr}^{-1}$. Innermost contours have highest magnitude. Note the close correlation between the extremal surface and maximum perturbation of melting rate ($|\Gamma'|$). (b) Map of W' interpolated onto the base of the melting region. Black lines show ridge segments, transform fault, Σ^+ and Σ^- . White lines show the trace of the extremal surfaces on the base of the melting region. Both figures are generated from the same simulations. $U_r = U_0 = 1 \text{ cm yr}^{-1}$. Ridge is migrating to the left in both cases.

thickening of the oceanic lithosphere with age causes the base of the lithosphere to have a curved shape in the cross axis direction. Consequently the average age of the lithosphere in the simulation domains, and hence cross axis curvature of the base of the lithosphere, decreases with spreading rate. Decreasing the curvature of the base of the lithosphere has the effect of increasing $|W'|$ (and $|\Gamma'|$) at all depths. Subsequently, the difference in the amount of melt focused from Σ^+ and Σ^- to the ridge segments at constant offset also increases with spreading rate.

In Figure (??), notable separation exists between all curves except those for $U_r = U_0 = 4 \text{ cm yr}^{-1}$ and $U_r = U_0 = 6 \text{ cm yr}^{-1}$. The volume (V) created by seafloor spreading for melt from the focusing regions to occupy is

$$V = 2U_0 t_c L, \quad (27)$$

where t_c is crustal thickness and L is the distance over which melt is distributed. At all offsets studied, the difference in the amount of melt focused from the Σ^+ and Σ^- to the ridge segments increases by approximately one third from simulations prescribed $U_r = U_0 = 4 \text{ cm yr}^{-1}$ to those where $U_r = U_0 = 6 \text{ cm yr}^{-1}$. This is offset by the change in V , which also increases by one thirds between simulations where $U_r = U_0 = 4 \text{ cm yr}^{-1}$ and $U_r = U_0 = 6 \text{ cm yr}^{-1}$.

The asymmetry of the perturbed flow about the ridge axis (Figure ??c) can also be explained by considering the effect of the lithosphere on mantle flow far from the transform fault. Ridge migration increases the strain rate beneath the leading plate relative to comparable points beneath the trailing plate by a factor of 0.2. This causes the leading plate to be thinner than the trailing plate, which causes $|W'|$ to be higher beneath the leading plate.

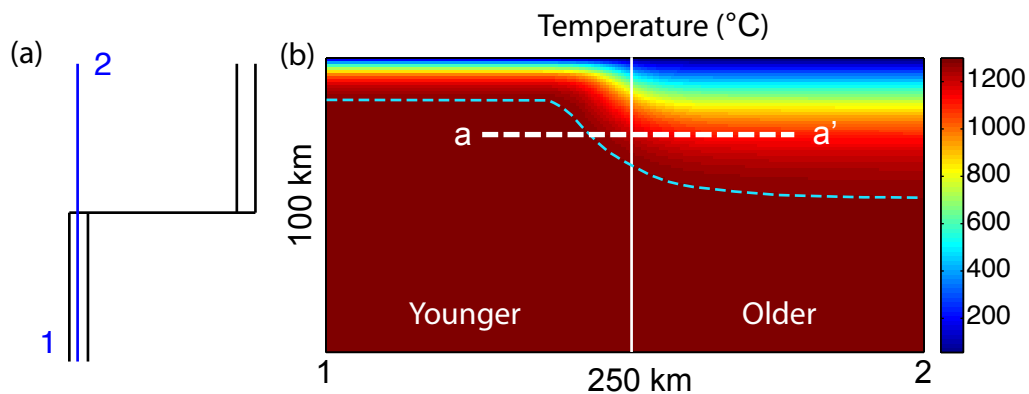


Figure 11: (a) Schematic ridge system geometry. (b) 2D slice showing temperature taken between 1 and 2 in (a). Profile generated from a simulation with $U_r = U_0 = 1 \text{ cm yr}^{-1}$, offset = 80 km. Thin vertical white line in centre of profile marks the position of the transform fault. Dashed blue line marks on the approximate base of the lithosphere. A temperature difference exists between positions a and a' , despite the points being at the same depth. The temperature difference causes cooling of the younger lithosphere on the left hand side of the transform fault in the figure and heating of the older lithosphere on the cooler right hand side. The temperature difference between two corresponding points on either side of the transform fault demonstrates the thermal edge effect.

5.3 Asymmetry Generated Near Transform Faults

Figure (??) illustrates how the thermal structure of the lithosphere differs on either side of a transform fault. Diffusion of heat across the transform fault works to cool the younger lithosphere and heat the older lithosphere. By altering the viscosity, heat diffusion thins the older lithosphere close to the transform fault and thickens the younger lithosphere. The thickness of the lithosphere is further modified by the strain rate associated with plate kinematics. The change in viscosity regime is known as the *edge effect*. The principle difference between the 3D and 2D simulations is the ability to simulate the edge effect.

Figures (?? and ??) give examples of how the edge effect modifies the shape of the melting region and lithosphere. Simulations predict that the edge effect induces along axis components of curvature to the melting region and lithosphere over distances up to 50 km from the transform fault. Components of along axis curvature increase W' (and hence Γ')

by a small positive amount and add an along axis component of velocity to the perturbed flow.

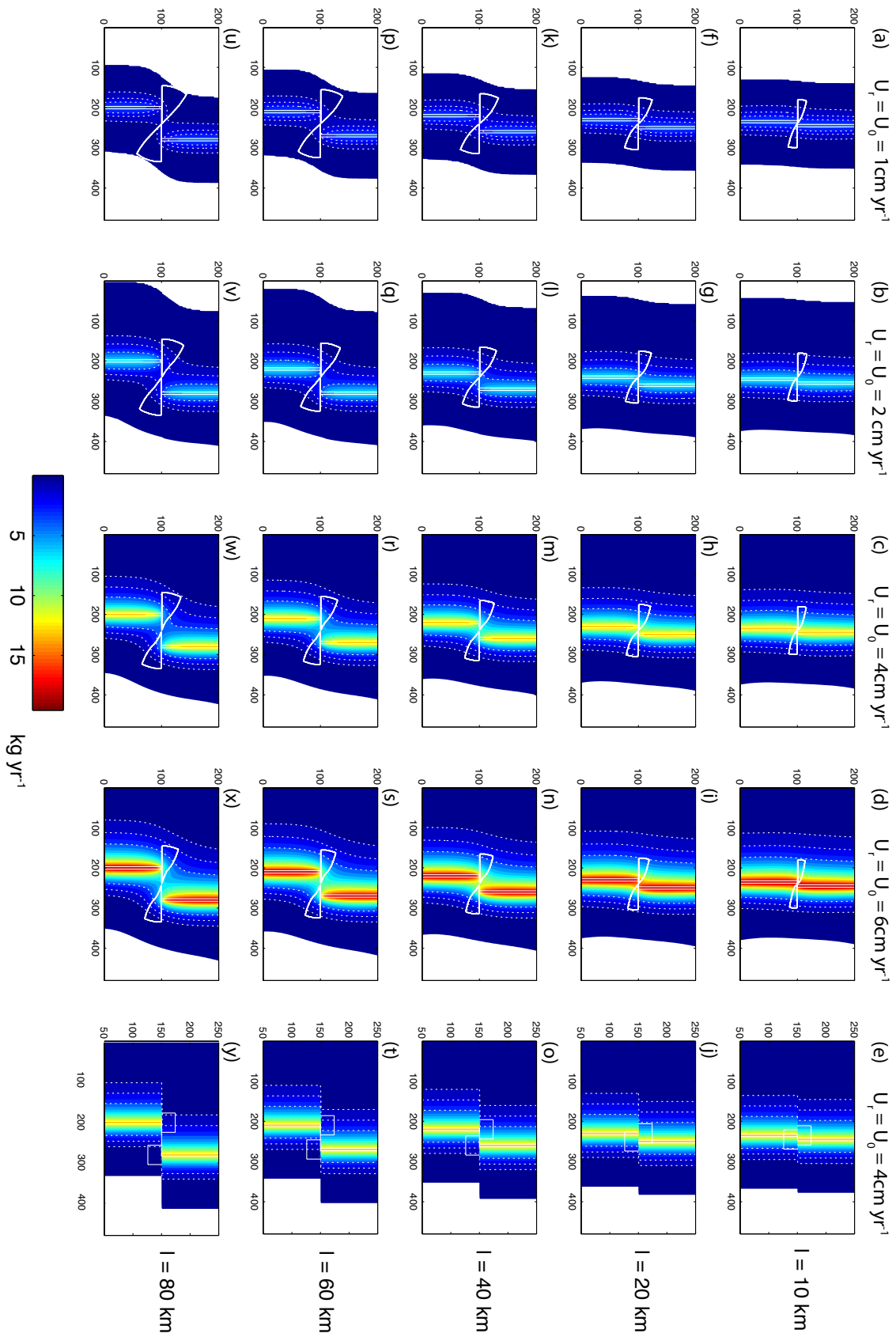
5.4 The Influence of Spreading Rate and Offset on the Edge Effect

The influence of the edge effect on simulation results is summarised in Figure (12), which shows how Γ_1 varies between simulations. For comparison, the melting rate predicted by 2D simulations has also been included. The influence of the edge effect can be broken down into two components (*i*) that controlled by spreading rate, (*ii*) that controlled by offset. However, it must be appreciated that simulation results (e.g. Figures ??, ??) are the consequence a competition between spreading rate and offset to modify the shape of the base of the lithosphere.

Figure 12: Contour maps coloured for the vertically integrated melting rate (Γ_1) for all simulated offsets (l) and spreading rates ($U_r = U_0$). White solid lines mark position of ridges, transform fault and focusing regions. White dashed lines highlight contours between regions that have similar colours. Right most column is generated from 2D simulation results. Ridge system is migrating to the left in all cases.

At constant offset, as $U_r = U_0$ increases, the thermal structure of the lithosphere either side of the transform fault becomes increasingly similar. This reduces the along axis distance over which the edge effect is felt. Consequently, spreading rate works to decrease the along axis extent of the regions Σ^+ and Σ^- (e.g. Figures 12 u, v, w, x). By reducing the distance over which the edge effect is felt, increasing spreading rate also increases the rate of change of W' , Γ' and Γ_1 across the transform fault.

At constant $U_r = U_0$, the along axis distance over which the edge effect is felt increases with offset. This forces the rate of change of W' , Γ' and Γ_1 across the transform fault to



increase with offset. The offset is responsible for controlling the cross axis extent of the regions Σ^+ and Σ^- . At all offsets, the maximum extent of Σ^+ and Σ^- in the direction pointing away from the ridge segments is one focusing distance (h). However the extent of Σ^+ and Σ^- on the transform fault side of the ridge axis is constrained to the smaller of either h or half of the total offset. Consequently, the area of Σ^+ and Σ^- increases with offset at fixed $U_r = U_0$ up to offset lengths of $2h$. The area of the focusing sub-regions decreases with further increases in offset.

5.5 Lithospheric Control on Peak Morphological Asymmetry

Figure (??) demonstrates the striking similarity between the shape of depth contours for the base of the lithosphere and the shape of the extremal surfaces. The extremal surfaces detail the location of maximum $|W'|$ at all depths within the domain. This similarity of shape indicates that the position and morphology of the extremal surfaces is controlled by the shape of the base of the lithosphere in the simulations run.

Mantle flow is subjected to a component of rotation about a vertical axis within a 50 kilometre wide zone either side of the transform fault. When the motion on the transform fault is left lateral, anticlockwise rotation occurs beneath the tip of the leading segment and transform fault, whilst clockwise rotation occurs beneath the tip of the trailing segment. The intensity of rotation increases with proximity to the base of the lithosphere. At deeper depths, rotation becomes weaker and more diffuse. It is not yet understood how rotation of the mantle affects the morphology and spatial position of the extremal surfaces. The offset at which the magnitude of morphological asymmetry peaks (Figure ??) does not reflect a single process. Instead, it ultimately results from complex interactions between spreading rate, rate of ridge migration and offset length that modify the shape of the base of the lithosphere and melting region.

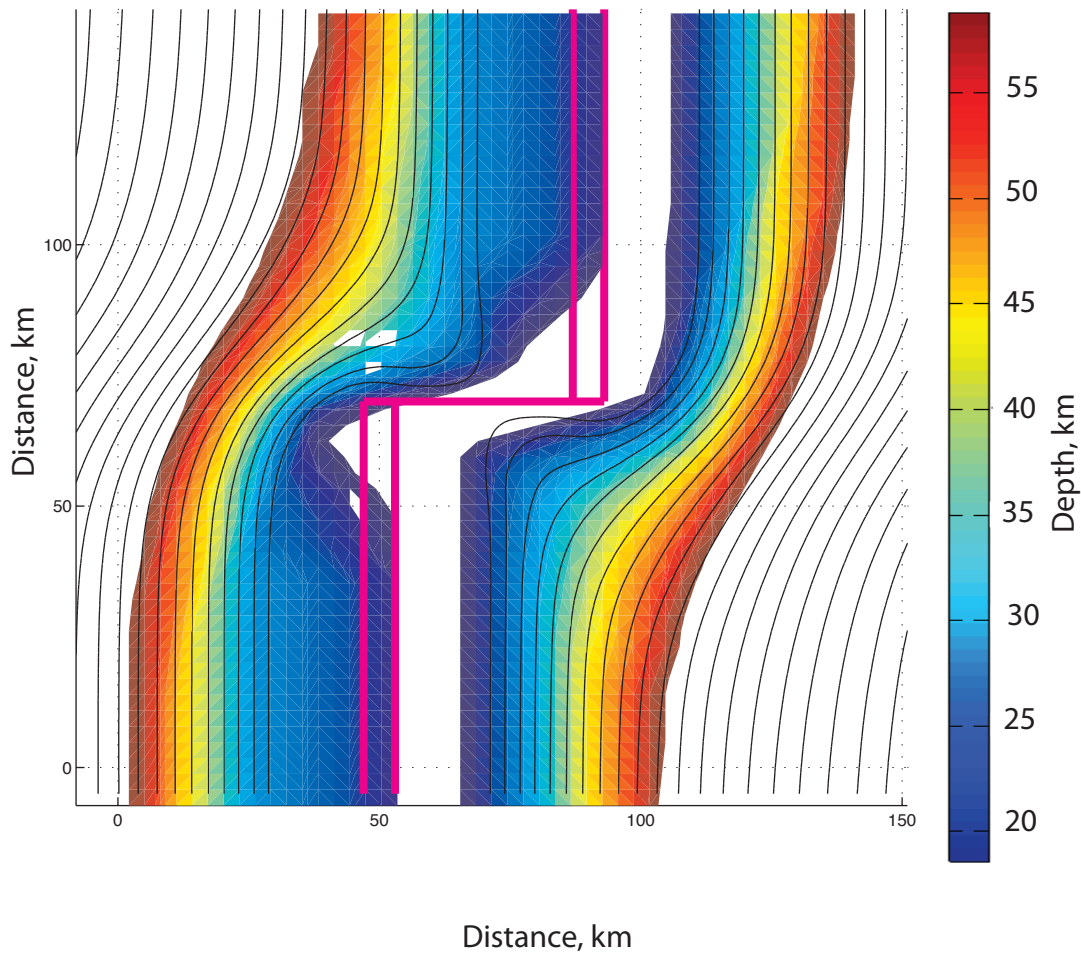


Figure 13: Relationship between shape of the base of the lithosphere and shape of the extremal surfaces. Extremal surfaces are coloured according to depth. Contours are spaced and 1 km intervals. Shallowest contour is 10 km. Ridge system shown by magenta lines. $U_r = U_0 = 4 \text{ cm yr}^{-1}$. Ridge is migrating to the left.

The curves of morphological asymmetry in Figure (??) are asymmetrical about their peak. This stems from the rate of change of W' and Γ' about the extremal surfaces. The magnitude of the average rate of change of W' (and hence Γ') with distance from the extremal surface is greatest on the ridge side of the surface. This causes the magnitude of the rate of change of difference in axial depth with offset to be greatest at offsets less than that at

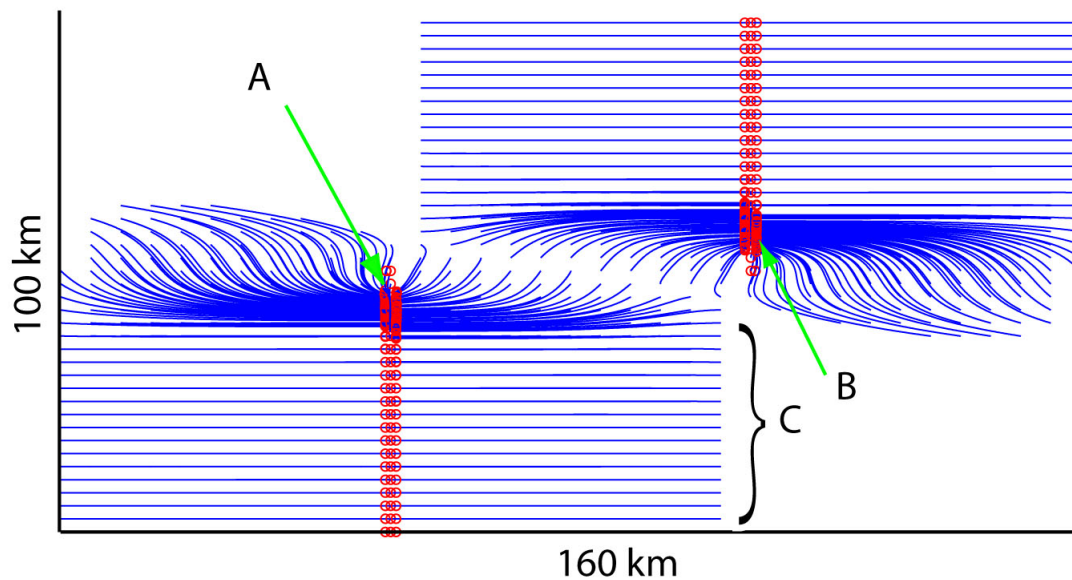


Figure 14: Blue streamlines show the trajectory of melt on the surface of the melting region during the focusing process. Red circles indicate the positions at which the streamlines cross into the crustal generation region. The crustal generation region is defined as the zone in which melt is segregated from the mantle into the crust. Positions A, B and C are referred to in the text.

which morphological asymmetry peaks.

5.6 Along Axis Crustal Thickness

Figure (??) shows the along axis crustal thickness predicted by the Streamline algorithm. The purpose of these profiles is to determine whether the melt focusing mechanism of ? predicts sensible variation of crustal thickness along the ridge axis. Unrealistic predictions of along axis crustal thickness could suggest that additional processes operate at shallow levels to redistribute melt along the ridge axis.

The shape of the crustal thickness profiles in Figure (??) can be explained by considering the behaviour of the streamlines (Section ??) in the focusing regions. Figure (??) gives a

representative example of the spatial behaviour of streamlines for an offset of 60 km. The streamlines run along the steepest local slope of the upper surface of the melting region, which approximates the high porosity channel of ?.

The small peak at the centre of the crustal thickness profiles in Figure (??) show where streamlines striking parallel to the ridge axis cross crustal generation region. Between the ridge-transform intersection and the point at which the melting region reaches its shallowest depth, few streamlines cross into the crustal generation region. This is shown by the large stretches of near-zero thickness crust close to the transform fault in Figure (??). This is indicated in Figure (??) as region (A).

When the melting region reaches its shallowest depth, streamlines are able to cross into the crustal generation region (region B in Figure (??)). Thick crust forms because streamlines are able to deliver melt to the ridge segment from the sub-regions Σ^+ and Σ^- and from positions either side of the ridge.

Slightly further away from the transform fault, the upper surface of the melting region attains constant depth in the along axis direction. Streamlines do not feel the edge effect induced by the transform fault and strike perpendicular to the ridge segment along their full length (region C in Figure ??). This ensures equal delivery of melt at all points along the axis in the direction pointing away from the transform fault. Consequently, constant crustal thickness is attained.

Figure (??) shows that the Streamline algorithm predicts an average crustal thickness of 3.4 km. This stems from several assumptions made in the construction of the numerical model. This implications of the model assumption are discussed in Section (??). The along axis crustal thickness profiles generated by the streamline algorithm are dissimilar

to observations from seismic studies (??),?. The dissimilarity between simulated and observed thickness indicates that the melt focusing mechanism of ? cannot solely account for the observed crustal morphology. Seismic studies (????) have revealed the presence of thin, narrow axial magma chambers beneath ocean spreading centres. Melt lenses are thought to sit on top of a crystal mush layer close to the bottom of the sheeted dyke layer beneath spreading segments. Lenses have also been imaged beneath mid-ocean ridge discontinuities.

? show that melt lenses beneath the $9^{\circ}03' N$ overlapping spreading centre on the East Pacific Rise are discontinuous. They suggest that the discontinuity of melt lenses prevents magma mixing between the eastern and western ridge segments at this location. However, they note that the separate magma reservoirs may share a common source. At the same overlapping spreading centre, ? demonstrate that a large melt anomaly occurs at the end of the ridge segments. They postulate that the melt anomalies arise from the same 3D focusing mechanism simulated by the Streamline algorithm used in this thesis. It is likely that melt sills represent a final melt pooling stage before shallow processes dominate and redistribute melt along the ridge segment.

It is possible to seismically image candidate shallow-level melt redistribution mechanisms. Normal faults are ubiquitous around the axial valley present at slow spreading mid-ocean ridges. Faults can act as conduits through which melt is extracted to the surface. Seismic and topographic profiles taken from the Lucky Strike volcano on the Mid-Atlantic ridge (??) show how a fault connects a topographic high within the axial valley to an underlying axial magma chamber.

? present results from a three dimensional tomographic study of a section of the Mid-Atlantic Ridge near the Oceanographer transform fault. Their 3D image shows $\simeq 10$

kilometre wide diapir-like low velocity anomalies within the crust. The anomalies spread out in the along and cross axis directions. ? are able to correlate the spatial location of the low velocity anomalies to the geographical position of volcanoes. They attribute the low velocity anomalies to lateral and vertical redistribution of melt through a network of dykes.

6 Discussion

6.1 Viscosity

Large variations in strain rate occur throughout the domain. Close to the transform fault and ridge segments $\dot{\epsilon} \approx 30 \times 10^{-14} \text{s}^{-1}$ when $U_r = U_0 = 6 \text{ cm yr}^{-1}$. However, $\dot{\epsilon}$ decays rapidly away from the transform fault to between $5 \times 10^{-14} \text{s}^{-1}$ and $10 \times 10^{-14} \text{s}^{-1}$. This is the typical range of strain rate values beneath the leading and trailing plates. The highest strain rates occur at very shallow depths ($< 10 \text{ km}$) beneath ridge segments. At such locations $\dot{\epsilon}$ can be in excess of $50 \times 10^{-14} \text{s}^{-1}$. Strain rates are much lower in analogous simulations run with $U_r = U_0 = 1 \text{ cm yr}^{-1}$. The spatial distribution and behaviour of strain rates remains much the same as for simulations run with $U_r = U_0 = 6 \text{ cm yr}^{-1}$. Despite this, strain rates in simulations where $U_r = U_0 = 1 \text{ cm yr}^{-1}$ are, on average, one order of magnitude less than those for $U_r = U_0 = 6 \text{ cm yr}^{-1}$.

Figure (??) shows that simulations run with the diffusion and dislocation creep dependent viscosity model create stronger morphological asymmetries than those run with the diffusion creep dependent viscosity model. This difference is caused principally by the strain rate dependence of the viscosity model. Viscosity scales inversely with $\dot{\epsilon}$. Accordingly, the topography of the base of the lithosphere, which controls the behaviour of W' and Γ' , will be exaggerated in simulations run with a non-Newtonian viscosity model relative to

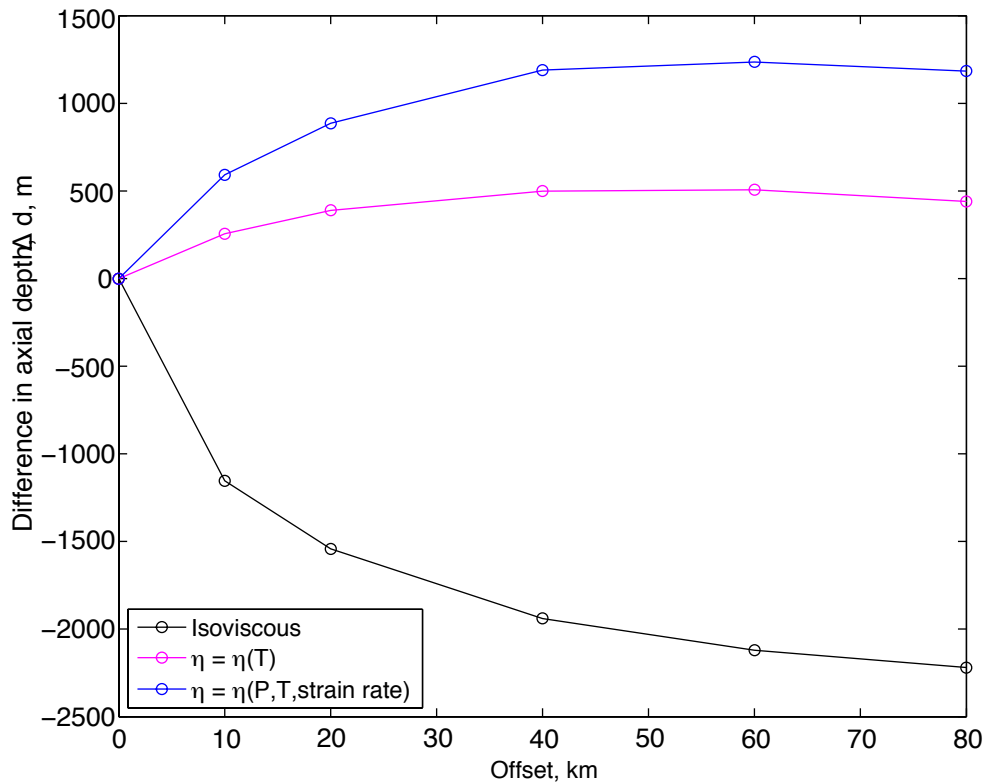


Figure 15: The magnitude of morphological asymmetry (Δd) depends strongly on the viscosity model used in the simulations. Negative values of Δd indicate that the depth to the trailing segment is less than the depth to the leading ridge segment. This is opposite to the trend observed by ?. Results are from simulations with $U_r = U_0 = 2 \text{ cm yr}^{-1}$. $\eta = \eta(T)$ shows results for simulations with a diffusion creep dependent viscosity model. Results from simulations with a diffusion and dislocation creep dependent viscosity are shown by the curve labelled $\eta = \eta(P, T, \text{strain rate})$.

those run with a strictly Newtonian viscosity model. Although Figure (??) only shows results for simulations run with $U_r = U_0 = 2 \text{ cm yr}^{-1}$, the difference in axial depth at all offsets between non-Newtonian and Newtonian simulations can be expected to increase with spreading rate. This is because the range of predicted $\dot{\epsilon}$ increases with spreading rate, thus causing greater variation in the topography of the base of the lithosphere. Consequently, greater variation in W' and Γ' is caused by increasing spreading rate.

Results from simulations run with a constant viscosity model in Figure (??) show the op-

posite asymmetry to that observed by ?. In this case the thermal boundary layer is not limited by high viscosity, leaving it free to be advected across the domain by the action of ridge migration. Cold material from beneath the leading plate is advected into the focusing sub-region Σ^+ , suppressing melting. Hot material is advected from beneath the leading ridge segment into Σ^- , augmenting melt production in this region. Consequently, the large negative morphological asymmetries shown in Figure (??) are created.

Layered viscosity models have been a popular choice for numerical and analytical models of mantle flow and melting beneath MORs and transform faults (e.g ??). In a layered viscosity model, ridge migration would result in advection of material across a portion of the domain as discussed above. The variable viscosity model used in this thesis highlights the sensitivity of $|W'|$ to the shape of the base of the lithosphere. Because layered viscosity models cannot accurately calculate the response of $|W'|$ to the shape of the base of the lithosphere, they are unsuitable for investigating the effect of ridge migration on mantle flow and melting.

6.2 Influence of Model Assumptions

Computational expense constrains the resolution, scale and complexity of numerical simulations of mantle flow and melting. The set of equations governing solid and liquid flow in the mantle have been derived by ?. This system of equations is too complex to be solved numerically in a large scale, high resolution domain. In order to isolate fundamental aspects mantle dynamics beneath a migrating ridge I use a more tractable set of governing equations. The governing equations (Equations ??, ??, ??) solve for incompressible flow of the solid mantle. Owing to assumptions made in the construction of the 3D numerical model, significant differences exist between simulation results and observed data.

Figure (??) shows that 3D simulations predict an average crustal thickness of 3.4 km when a reasonable focusing distance is used ($h = 55\text{km}$). This value contrasts strongly with the observed crustal thickness of 7 ± 1 km (e.g. ?). The 3D model underestimates the amount of melt produced beneath and focused to a MOR segment. Modelling and experimental studies estimate the melt fraction needed for MORB genesis to be between 15% and 30% (??). Contrastingly, the 3D model used here predicts the melt fraction to be approximately 10%. By solving for incompressible flow, the model assumes that no material is removed from the mantle by melting. However, that mass extraction from the mantle through melting occurs is demonstrated by the ubiquity of oceanic crust at all mid-ocean ridges within the range of spreading rates studied (?). Owing to this, mantle flow within the solidus must be compressible. Therefore, the flux of solid mantle into the melting region is greater in a compressible mantle than in an incompressible mantle at a given $U_r = U_0$. Provided that the adiabatic productivity is the same in both cases, compressible flow models will predict a higher melt fraction than models simulating incompressible flow. It is likely that a significant fraction of the difference between the predicted and observed crustal thicknesses results from the condition of incompressibility.

Computational expense prevents the model from simulating thermodynamically governed mantle melting at the scale and resolution required by these simulations. Beneath the solidus, upwelling material is moved along the mantle adiabat. Melting begins when the upwelling rock migrates into the melting region. The latent heat needed to melt the rock is sourced from the internal energy of the upwelling rock. This causes the temperature of mantle material to decrease more rapidly than it would along the solid and liquid adiabats (?). The governing equations do not account for change in the mantle's thermal structure induced by melting. It is difficult to predict how inclusion of the latent heat of melting in the model would alter the simulation results.

6.3 Melt Focusing

Along axis variation in rare earth elements (REEs) may be used to better constrain the scale and geometry of along axis melt redistribution. Dy/Yb provides a good proxy for assessing the amount of melt originating from a deep garnet-rich source region (e.g. ???). Owing to Dy being much more incompatible in garnet than Yb (?), melt from a garnet-rich source will have a high Dy/Yb relative to shallow melts.

Figure (??) shows that the roof of the melting region is deeper within the focusing sub-regions Σ^+ and Σ^- than it is along the length of the ridge segment. Therefore, a higher proportion of melt originating from within Σ^+ or Σ^- will originate from a garnet source relative to melts produced along the ridge segment. Consequently, melts produced in Σ^+ or Σ^- can be expected to have higher Dy/Yb ratios than other melts produced in the domain. If profiles of Dy/Yb concentration were plotted along ridge segments, sharp pronounced peaks in Dy/Yb close to the transform fault will indicate little along axis redistribution of melt. Conversely, broad peaks in Dy/Yb close to transform faults may suggest significant along axis redistribution of melt. Alternatively, melt from different source regions may be mixed before it is sequestered into the crustal generation region.

? note that the higher Dy/Yb ratios are typically associated with the leading ridge segment. This arises because ridge migration ensures that the mantle melting within Σ^- has undergone previous melting whilst in Σ^+ . This depletes the mantle in Σ^- in Dy/Yb relative to that in Σ^+ . Further analysis of simulation results, coupled with a simple model of mantle Dy/Yb composition will allow the geochemical asymmetry generated by the 3D model to be evaluated in a similar way to the morphological asymmetry. In turn, this may be used to help refine estimates for the focusing distance.

7 Conclusions

The 3D numerical model described in this thesis shows that lithosphere-induced mantle dynamics can account for morphological variation observed along mid-ocean ridges (MORs). The component of mantle flow induced by ridge migration perturbs the melting rate throughout the sub-ridge mantle. This perturbation results in different amounts of melt being focused to ridge segments separated by an offset, causing morphological asymmetry between MOR segments. The behaviour of the component of flow induced by ridge migration is sensitive to the shape of the base of the lithosphere. Spreading rate, rate of ridge migration and offset length control the shape of the base of the lithosphere. The 3D simulations suggest that the maximum distance over which melt can be focused to the ridge segment is 55 km, assuming complete extraction of melt from the mantle. Previous work with 2D simulations of asthenospheric flow and melting estimated the focusing distance to be 24 km (?). The revised figure of 55 km is an improvement on the estimate provided by the 2D model and closely agrees with estimates based on dynamical and thermodynamical calculations of asthenospheric flow and melting (?).

2D simulations of mantle flow beneath migrating MORs are useful for investigating the scale of upwelling and melting at large distances from transform faults. However, 3D models are needed to capture the behaviour of mantle flow and melting near transform faults. It is necessary for numerical models of mantle flow and melting beneath mid-ocean ridges to employ a variable viscosity model. The asymmetry of melting rates between the focusing regions for adjacent ridge segments is enhanced by a factor of 2 or 3 by use of a non-Newtonian (dislocation creep and diffusion creep) viscosity model over a Newtonian (diffusion creep) viscosity model.

The size of the domain used is limited by computational expense. Further work is needed to understand how the magnitude of the melting rate perturbation scales with the simu-

lated asthenospheric depth. Geochemical data and simple models of mantle composition can be used with the 3D model to better understand the scale of the melt focusing and along axis redistribution of melt.

Appendices

A Notation

Variable	Meaning	Value used	Dimensions
x	Coordinate aligned with the cross axis direction		
y	Coordinate aligned with the along axis direction		
z	Coordinate aligned with the depth direction		
W	Vertical component of velocity		m s^{-1}
X	Physical extent of domain in the x direction		m
Y	Physical extent of domain in the y direction		m
Z	Physical extent of domain in the z direction		m
P	Dynamic pressure		Pa
T	Temperature		$^{\circ}\text{C}$
θ	Mantle potential temperature		$^{\circ}\text{C}$
η	Viscosity		Pa s^{-1}
$\dot{\epsilon}$	Strain rate		s^{-1}
κ	Thermal diffusivity	10^{-6}	m^2s^{-1}
h	Focusing distance		m
Γ	Melting rate		$\text{kg m}^{-3}\text{yr}^{-1}$
Γ_1	Vertically integrated melting rate $\int_0^Z \Gamma \text{d}z$		$\text{kg m}^{-2}\text{yr}^{-1}$
Δd	Difference in axial depth across ridge offsets		m
U_r	Rate of ridge migration		m s^{-1}
U_0	Half spreading rate		m s^{-1}

B Derivation of the Governing Equations

B.1 The Mass Conservation Equation

The mass conservation equation (Equation ??) is otherwise known as the continuity equation. Mass must be conserved because the model solves for incompressible fluid flow. Consider an arbitrary finite volume V viewed in Eulerian coordinate space. Fluid with density ρ moves in and out of the volume with velocity \mathbf{v} at points across the surface of the volume. Taking $d\mathbf{S}$ to be an element of the surface, where $|d\mathbf{S}|$ is the area of the element and its direction is the outward pointing normal, the component of \mathbf{v} parallel to $d\mathbf{S}$ is the velocity that transfers mass out of V . Therefore, the outward mass flux per unit time from the arbitrary volume V is $\rho \mathbf{v} \cdot d\mathbf{S}$. Consequently,

$$\text{rate of mass loss from } V = \int_S \rho \mathbf{v} \cdot d\mathbf{S} \quad (28)$$

$$\text{total mass in volume } V = \int_V \rho dV. \quad (29)$$

From Equations (?? and ??) we get

$$\frac{d}{dt} \int_V \rho dV = \int_V \frac{\partial \rho}{\partial t} dV = - \int_S \rho \mathbf{v} \cdot d\mathbf{S}. \quad (30)$$

focusing on conserving mass at a point, rather than throughout the whole of a finite volume renders the first term in Equation (??) redundant and reduces the rest to

$$\frac{\partial \rho}{\partial t} = - \lim_{V \rightarrow 0} \left[\int \rho \mathbf{v} \cdot \frac{d\mathbf{S}}{V} \right]. \quad (31)$$

Equation (??) can be reduced, by definition of the divergence operator, to

$$\frac{\partial \rho}{\partial t} = \nabla \cdot (\rho \mathbf{v}). \quad (32)$$

Assuming constant density, the continuity equation (??) reduces to the simple form

$$\nabla \cdot \mathbf{v} = 0 \quad (33)$$

B.2 The Navier Stokes Equation

An element of fluid of volume V , density ρ , and surface area ∂V , is subjected to velocity \mathbf{v} . A surface force results from traction \mathbf{t} , and gravity \mathbf{g} acts to provide a body force. Writing these into a force balance gives

$$\int_V \rho a_i dV = \int_V \rho g_i dV + \int_{\partial V} t_i dS \quad (34)$$

where a_i is acceleration. Substituting $t_i = \tau_{ij}n_j$ into (??), where τ_{ij} is the stress tensor and n_j is the normal to the surface traction is acting across, we get

$$\int_V \rho a_i dV = \int_V \rho g_i dV + \int_{\partial V} \tau_{ij}n_j dS \quad (35)$$

Applying the divergence theorem to equation (??) and dividing through by the volume V gives

$$\rho a_i = \rho g_i + \tau_{ij,j} \quad (36)$$

where $\tau_{ij,j} = d\tau_{ij}/dx_j$. In the Lagrangian frame of reference (coordinate frame moves with the fluid particle), the components of the small distance moved by the fluid particle in time δt (in the limit of $\delta t \rightarrow 0$) are δx , δy , and δz . The acceleration of the particle can be written as

$$\mathbf{a} = \frac{D\mathbf{v}}{Dt} = \frac{\partial \mathbf{v}}{\partial t} + u \frac{\partial \mathbf{v}}{\partial x} + v \frac{\partial \mathbf{v}}{\partial y} + w \frac{\partial \mathbf{v}}{\partial z} \quad (37)$$

where $\mathbf{v} = (u, v, w)$. In suffix notation this is simply $a_i = \dot{v}_i + v_j v_{i,j}$. By substituting equation (??) into (??) we can write the rate of change of momentum of a fluid particle

more fully as

$$\rho v_j v_{i,j} + \rho \frac{\partial v_i}{\partial t} = \rho g_i + \tau_{ij,j}. \quad (38)$$

Newton's law for a viscous fluid states

$$\tau_{ij} = -P\delta_{ij} + 2\mu\dot{\epsilon}_{ij} \quad (39)$$

where $\dot{\epsilon}_{ij}$ is the strain rate tensor and μ is the viscosity.

$$\dot{\epsilon}_{ij} = \frac{1}{2}(v_{i,j} + v_{j,i}). \quad (40)$$

Substituting equations (??) and (??) into (??) gives the Navier Stokes equation:

$$\rho v_j v_{i,j} + \rho \dot{v}_i = \rho g_i + -[P\delta_{ij} + \mu(v_{i,j} + v_{j,i})]_{,j}, \quad (41)$$

or

$$\mathbf{v} \cdot \nabla \mathbf{v} + \frac{\partial \mathbf{v}}{\partial t} = -\frac{1}{\rho} \nabla P + \frac{1}{\rho} \nabla \cdot [\mu (\nabla \mathbf{v} + \nabla \mathbf{v}^T)] + \mathbf{g}. \quad (42)$$

B.3 Stokes Flow

Assuming steady state flow and negligible contribution from the body force, the Navier Stokes equation can be simplified to

$$\rho \mathbf{v} \cdot \nabla \mathbf{v} = -\nabla P + \nabla \cdot [\mu (\nabla \mathbf{v} + \nabla \mathbf{v}^T)]. \quad (43)$$

The first term in this equation is the inertial term, the second is the pressure force and the third is the viscous force. In the case of viscous fluids, the viscous terms dominate over the inertial terms. Where U and L are velocity and length scales respectively, this can be

represented by considering the Reynolds number of the fluid

$$Re = \frac{\text{inertial terms}}{\text{viscous terms}} \sim \frac{\rho UL}{\mu} \quad (44)$$

By non-dimensionalising the simplified momentum equation (??) we can make a further simplification that is applicable to viscous fluids. We define dimensionless variables, indicated by primes

$$\mathbf{x} = L\mathbf{x}', \quad \mathbf{v} = U\mathbf{v}', \quad m = Mm', \quad t = Tt'. \quad (45)$$

Here L is a characteristic length scale, equal to the length of the domain the equations are solved in. U is a characteristic velocity scale. Like the length scale, this is a constant and takes the value of the half spreading rate of the ridge system. M and T are characteristic mass and time scales respectively. Using these quantities, it is possible to non-dimensionalise pressure, density and the differential operator ∇

$$P = \frac{M}{LT^2}, \quad \rho = \frac{M}{L^3}, \quad \nabla = \frac{1}{L} \nabla'. \quad (46)$$

In terms of the non-dimensional variables, the Navier Stokes equation in the absence of body forces and under steady state conditions becomes

$$\frac{U^2}{L} \mathbf{v}' \cdot \nabla' \mathbf{v}' = -\frac{L}{T^2} \frac{1}{\rho'} \nabla' P' + \nabla' \cdot \left[\frac{U}{T} \frac{\mu'}{\rho'} (\nabla' \mathbf{v}' + \nabla' \mathbf{v}'^T) \right] \quad (47)$$

Dividing through by U^2/L and substituting in equation (??) with μ and ρ in their non-dimensional form yields

$$\mathbf{v}' \cdot \nabla' \mathbf{v}' = -\frac{1}{\rho'} \nabla' P' + \nabla' \cdot \left[\frac{1}{Re} (\nabla' \mathbf{v}' + \nabla' \mathbf{v}'^T) \right]. \quad (48)$$

In the limit $Re \rightarrow 0$ (applicable for highly viscous fluids), the inertial term can be neglected and a dominant balance exists between the viscous and pressure gradient forces.

From equation (??) we get

$$0 = -\frac{1}{\rho'} \nabla' P' + \nabla' \cdot \left[\frac{1}{Re} (\nabla' \mathbf{v}' + \nabla' \mathbf{v}'^T) \right]. \quad (49)$$

Reverting to the dimensional form and considering the dimensional form of equation (??) with (??) we find

$$\nabla P = \nabla \cdot [\mu (\nabla \mathbf{v} + \nabla \mathbf{v}^T)] \quad s.t. \quad \nabla \cdot \mathbf{v} = 0. \quad (50)$$

B.4 Advection and Diffusion of Heat

Conduction, diffusion and advection of heat give rise to variations in the viscosity and density of the sub-ridge mantle. The Boussinesq approximation states that density variations can be neglected except in the buoyancy term, where they are multiplied by g . Making the further assumption that buoyancy forces are negligible allows all density variations to be neglected. This assumption is reasonable provided that all accelerations in the flow are small compared with $|g|$ (i.e. $|D\mathbf{u}/Dt| \ll |g|$). For the Boussinesq approximation to be valid and accurate the ratio of difference in densities, $\Delta\rho$ to a reference density, ρ_o is of the order unity (i.e. $\nabla\rho/\rho_o \ll 1$). The effect of temperature on density can be linearised in these circumstances: mod g

$$\Delta\rho = -\alpha\rho_o\Delta T \quad (51)$$

For rock, $\alpha \simeq 10^{-5} K^{-1}$. From this we can see that even with temperature variations on the order of 10^3 K, $\Delta\rho/\rho \ll 1$. Applying the Boussinesq approximation and assuming that the specific heat capacity at constant pressure, C_p is uniform throughout the domain, $\rho C_p DT/Dt$ is equal to the rate of heating per unit volume of material. A thermal equation can be obtained by modifying the Navier Stokes equation. Heating of mantle material is brought about by transfer of thermal energy from neighbouring fluid particles by thermal conduction and, sometimes through internal heat generation, for example, through decay of radionuclides. These conduction and internal heat generation terms are analogous to the viscous and body force terms of the Navier Stokes equation. The conductive heat flux is

$$\mathbf{H} = -k\nabla T, \quad (52)$$

where k is the thermal conductivity of rock. Therefore

$$\rho C_p \frac{DT}{Dt} = -\nabla \cdot \mathbf{H} + J \quad (53)$$

where J is the rate of internal heat generation per unit volume. Taking k to be constant throughout the domain equation (53) can be rewritten

$$\frac{\partial T}{\partial t} + \mathbf{v} \cdot \nabla T = \kappa \nabla^2 T + \frac{J}{\rho C_p} \quad (54)$$

where

$$\kappa = \frac{k}{\rho C_p}. \quad (55)$$

where κ is the thermal diffusivity. Assuming there is no internal heat generation, and applying the existing assumption that the system is at steady state, equation (54) reduces to

$$\mathbf{v} \cdot \nabla T = \kappa \nabla^2 T \quad (56)$$

C Melt Focusing Algorithms

C.1 Streamline Focusing Algorithm

```

function rs = streamAnalysisMeshBeta(rs, fdist)

% FUNCTION rs = streamAnalysisMeshBeta(rs,fdist)
%
% rs = simulation, fdist = focusing distance (km).
%
% function calculates how melt is focused to the ridge segment by
% plotting streamlines from cells lying within the focusing distance
% from the ridge (fdist). Streamlines are defined by the gradient of
% the melting region. Streamlines that originate from a position
% outside of the y-dimensions of the ridge (i.e. one of the omega
% areas defined in Katz et al 2004) are used to work out the mass of
% melt and thickness of crust distributed over the first 1km of the
% ridge segment. These values are represented in rs.melt.M,
% rs.melt.C and rs.melt.D, allowing direct comparison of this
% streamline algorithm with the nearest neighbour and simple
% (2D) focusing algorithms.

[xr yr] = getRidgePosVector(rs);
full_rate = 2 * rs.par.half_rate * 1e-2; % (m)
rho_c = 2900; % density of crust (kg /m^3)
dx = 1; % y-grid spacing
dy = 1; % x-grid spacing (km)

% Meshgrid fields and include bcs
% sv = gradient of solidus in y direction
% su = gradient of solidus in x direction
% ga is the melting rate field
% ga_zi is the vertically integrated melting rate
[Xo Yo] = meshgrid(rs.coord.x, rs.coord.y);
suMesh = interp2(Xo,Yo,rs.melt.su,1:max(rs.coord.x),...
[1:max(rs.coord.y)]', 'linear');
svMesh = interp2(Xo,Yo,rs.melt.sv,1:max(rs.coord.x),...
[1:max(rs.coord.y)]', 'linear');
gaMesh = interp2(Xo,Yo,rs.melt.ga_zi,1:max(rs.coord.x),...
[1:max(rs.coord.y)]', 'linear');

if rs.par.periodic == 0
% if the simulation is non-periodic
% i.e. reflection condition on y boundary
svMesh = [svMesh(1,:); svMesh; svMesh(end,:)];
suMesh = [suMesh(1,:); suMesh; suMesh(end,:)];
gaMesh = [gaMesh(1,:); gaMesh; gaMesh(end,:)];
else
svMesh = [svMesh(end,:); svMesh; svMesh(1,:)];
suMesh = [suMesh(end,:); suMesh; suMesh(1,:)];
gaMesh = [gaMesh(end,:); gaMesh; gaMesh(1,:)];
end

```

```

clearvars Xo Yo;

% Calculate streamlines and focused melt
%Initialise arrays
arrsize = size(gaMesh);
interceptMelt = zeros(arrsize(1), arrsize(2), ceil(length(xr)/2));
rs.melt.streamM = zeros(1,ceil(length(xr)/2));
rs.melt.startPlotterL = zeros(arrsize(1), arrsize(2));
rs.melt.startPlotterT = zeros(arrsize(1), arrsize(2));
rs.melt.startCounter = [0 0];
[X Y] = meshgrid([1:rs.par.width],[0:rs.par.length+1]);

for i = 2:2:length(xr) %loop over ridge segments
    xrr = [xr(i-1) xr(i)];
    yrr = [yr(i-1) yr(i)];
    for j = 1:arrsize(2)
        for k = 2:arrsize(1)-1
            y = Y(k,1); x = X(1,j);
            % if grid cell is within 1 fdist of the ridge
            if (x ≤ max(xrr) + fdist && x ≥ min(xrr) - fdist &&...
                (max(yrr) ≠ min(yrr)))
                str = stream2(X,Y,suMesh,svMesh,x,y,[0.1 1600]);
                seg = focusedToSegment(rs, str, xrr, yrr, dx, dy, ...
                    fdist,i);
            end
        end
    end
    % if ridge segment is trailing
    if (seg(1) == 1 && round(i/4)==i/4 && (str{1}(1,2)...
        < min(yrr)))
        %calculate mass of melt focused from focusing region
        rs.melt.streamM(1,i/2) = rs.melt.streamM(1,i/2) + ...
            (gaMesh(seg(2), seg(3))...
                * dx * dy * 1e6);
        rs.melt.startCounter(1) = rs.melt.startCounter(1)+1;
        rs.melt.startPlotterT(seg(2),seg(3)) = 1;
    %else if the segment is leading
    elseif (seg(1) == 1 && round(i/4) ≠ i/4 && ...
        (str{1}(1,2) > max(yrr)))
        rs.melt.streamM(1,i/2) = rs.melt.streamM(1,i/2) + ...
            (gaMesh(seg(2), seg(3)) * dx * dy * 1e6);
        rs.melt.startCounter(2) = rs.melt.startCounter(2)+1;
        rs.melt.startPlotterL(seg(2), seg(3)) = 1;
    end
end
end

% Convert streamM to crustal thickness and change in axial depth
rs.melt.streamC = rs.melt.streamM ./ (full_rate * 1e3 * rhoc);
rs.melt.streamD = rs.melt.streamC .* 0.17;

% Calculate the along axis crustal thickness
rs.melt.hiResCrust = squeeze(sum(interceptMelt,2)) ./ ...
    (full_rate * rhoc * 1e3);

function seg = focusedToSegment(rs, str, xrr, yrr, dx, dy, fdist,ridge)

```

```

x = str{1}(:,1);
y = str{1}(:,2);
seg = zeros(7,1);
xtol = dx; ytol = dy * 0.1;
d = distanceFromSeg(x(1),y(1),xrr,yrr,fdist);

if (isempty(d) == 0 && d ≤ fdist)
    xi = find(x ≥ (min(xrr) - xtol) & x ≤ (max(xrr) + xtol));
    yi = find(y ≥ (min(yrr) - ytol) & y ≤ (max(yrr) + ytol));
    int = intersect(xi,yi);
    xint = x(min(int)); % gives spatial position of intersection
    yint = y(min(int));

    if (isempty(int) == 0) % i.e. if there IS intesection and focusing
        seg(1) = 1;
        seg(2) = y(1) / dy+1; % position melt is focused from
        seg(3) = x(1) / dx;
        seg(4) = round(yint / dy);
        seg(5) = round(xint / dx);
        seg(6) = yint;
        seg(7) = xint;
    end
end

```

```
function d = distanceFromSeg(x,y,xrr,yrr,fdist)
```

```

xs = abs(x - max(xrr))^2;
ymaxs = abs(y - max(yrr))^2;
ymins = abs(y - min(yrr))^2;

if (y ≤ max(yrr) && y ≥ min(yrr) && ...
    ((abs(x) - max(xrr)) ≤ fdist))
    d = abs(x - max(xrr));
elseif (y > max(yrr))
    d = sqrt(xs + ymaxs);
elseif (y < min(yrr))
    d = sqrt(xs + ymins);
else
    d = [];
end

```

```
function [xr, yr] = getRidgePosVector(rs)
```

```

xr = [];
yr = [0];
for i = 1:7
    rp = ['rpos',num2str(i)];
    tp = ['tpos',num2str(i)];
    if (isfield(rs.par,rp))
        xr = [xr,getfield(rs.par,rp), getfield(rs.par,rp)];
    end
    if (isfield(rs.par,tp));
        yr = [yr,getfield(rs.par,tp), getfield(rs.par,tp)];
    end
end

```

```

    end
end
xr = xr * rs.par.Lscale;
yr = [yr, yr(end)] * rs.par.Lscale;

```

C.2 Rectangular Focusing Algorithm

```

function rs = simpleAnalysisMesh(rs, fdist)

% FUNCTION simpleAnalysisMesh creates a fine 1 x 1km mesh and
%lays it over the regions of rs.melt.ga_zi that are focused to the ridge.
% It interpolates the values of rs.melt.ga_zi.

[xr, yr] = getRidgePosVector(rs);

%Define parameters and initialise array.

rs.melt.simpleM = zeros(1, length(xr)/2);
full_rate = 2 * rs.par.half_rate * 1e-2; %m
rhoc = 2900; %kg /m^3
L = 1e3; % distance over which melt is distributed (m)

% Integrate over the focusing area
for i = 2:2:length(xr)
    xrr = [xr(i-1) xr(i)];
    yrr = [yr(i-1) yr(i)];
    [X, Y] = meshgrid(rs.coord.x, rs.coord.y);
    if (max(yrr) - min(yrr) ≠ 0) %outside j dimension of ridge
    if ((round(i/4) - i/4 ≠ 0)) %if ridge segment is leading
        Z = interp2(X, Y, rs.melt.ga_zi, ...
            ((min(xrr) - fdist):1:(min(xrr)+fdist)), ...
            (max(yrr):1:(max(yrr)+fdist))');
        rs.melt.simpleM(1, i/2) = sum(sum(Z, 2)) * 1e6;
    else %ridge segment is trailing

        Z = interp2(X, Y, rs.melt.ga_zi, ((min(xrr) - ...
            fdist):1:(min(xrr)+fdist)), ...
            ((min(yrr)-fdist):1:min(yrr))');
        rs.melt.simpleM(1, i/2) = sum(sum(Z, 2)) * 1e6;
    end
end
end

%convert simpleM to crustal tthickness, C and isostatically
% compensate (D)
rs.melt.simpleC = rs.melt.simpleM ./ (full_rate * rhoc * L);
rs.melt.simpleD = rs.melt.simpleC .* 0.17;

function [xr, yr] = getRidgePosVector(rs)

xr = [];
yr = [0];
for i = 1:7
    rp = ['rpos', num2str(i)];

```

```

    tp = ['tpos', num2str(i)];
    if (isfield(rs.par, rp))
    xr = [xr, getfield(rs.par, rp), getfield(rs.par, rp)];
    end
    if (isfield(rs.par, tp));
    yr = [yr, getfield(rs.par, tp), getfield(rs.par, tp)];
    end
end
xr = xr * rs.par.Lscale;
yr = [yr, yr(end)] * rs.par.Lscale;

```

C.3 Half-Circle Focusing Algorithm

```

function rs = nearestAnalysisMeshBeta(rs, fdist)

% Integrates the vertically integrated melting rate over a
% half-circle focusing region to calculate the asymmetry in
% the amount of melt focused to the ridge segments from the
% focusing regions

[xr, yr] = getRidgePosVector(rs);
rhoc = 2900; % density of crust (kg/m^3)
dx = 1; % interpolated grid spacing (km)
dy = 1; % interpolated grid spacing (km)
L = 1e3; % distance over which melt is
%distributed (m)
full_rate = 2 * rs.par.half_rate * 1e-2; % full spreading rate (m/yr)

[X, Y] = meshgrid(rs.coord.x, rs.coord.y);
x = 1:1:rs.par.width;
y = 1:1:rs.par.length;
%ga_zi = rs.melt.ga_zi;
ga_zi = interp2(X, Y, rs.melt.ga_zi, x, y, 'spline');
% initialise arrays
rs.melt.nearestM = zeros(1, length(xr)/2);
rs.melt.sum = zeros(1, length(xr)/2);
a = zeros(size(ga_zi));

% loop over ridge segments
for k = 2:2:length(xr)
    xrr = [xr(k-1) xr(k)];
    xrr = round(xrr);
    yrr = [yr(k-1) yr(k)];
    omega = zeros(size(ga_zi));

    % create masks (omega) for focusing regions
    if ((round(k/4) ≠ k/4) && (max(yrr) ≠ min(yrr)))
% segment is leading and point lies outside
% y dimension of ridge
        for i = ((min(xrr) - fdist):1:(min(xrr)+fdist))
            for j = (max(yrr):1:(max(yrr)+fdist))
                if j>max(yrr)
                    x = abs(i - min(xrr));
                    y = abs(j-max(yrr));

```

```

        d = sqrt(x^2 + y^2);
        if (d<fdist)
            omega(j,i) = 1;
        end
    end
end
end
elseif (round(k/4) == k/4 && (max(yrr) ≠ min(yrr)))
% segment is trailing and point lies outside y
% dimension of the ridge
for i = ((min(xrr)-fdist):1:(min(xrr)+fdist))
    for j = ((min(yrr)-fdist):1:min(yrr))
        if j<min(yrr)
            x = abs(i-min(xrr));
            y = abs(j-min(yrr));
            d = sqrt(x^2+y^2);
            if (d<fdist)
                omega(j,i) = 1;
            end
        end
    end
end
end
end

% calculate amount of focused melt (kg /yr) (nearest.M)
focused = omega .* ga_zi;
rs.melt.sum(1,k/2) = sum(sum(omega,2));
rs.melt.nearestM(1,k/2) = sum(sum(focused,2)) .* (1e6 * dx * dy);
a = a+omega;
end

% Convert mass of melt to crustal thickness (C) and axial depth(D)
rs.melt.nearestC = rs.melt.nearestM ./ (rhoc * full_rate * L);
rs.melt.nearestD = rs.melt.nearestC .* 0.17;

```

```
function [xr, yr] = getRidgePosVector(rs)
```

```

xr = [];
yr = [0];
for i = 1:7
    rp = ['rpos', num2str(i)];
    tp = ['tpos', num2str(i)];
    if (isfield(rs.par, rp))
        xr = [xr, getfield(rs.par, rp), getfield(rs.par, rp)];
    end
    if (isfield(rs.par, tp));
        yr = [yr, getfield(rs.par, tp), getfield(rs.par, tp)];
    end
end
xr = xr * rs.par.Lscale;
yr = [yr, yr(end)] * rs.par.Lscale;

```

D Parallel Performance of the 3D Code

The program is memory intensive. When the problem size exceeds 50000 degrees of freedom per processor, performance is sharply degraded. Although PETSc provides the program with inherent parallelism, perfect scaling with between the problem run time and increasing number of processors is not guaranteed. Figure (??) shows how the run time of the code scales with the number of processors used, compared to ideal scaling. This scaling study shows that the code remains efficient when distributed across a number of processors. Simulations run for this study each took approximately 10 hours on 128 processors.

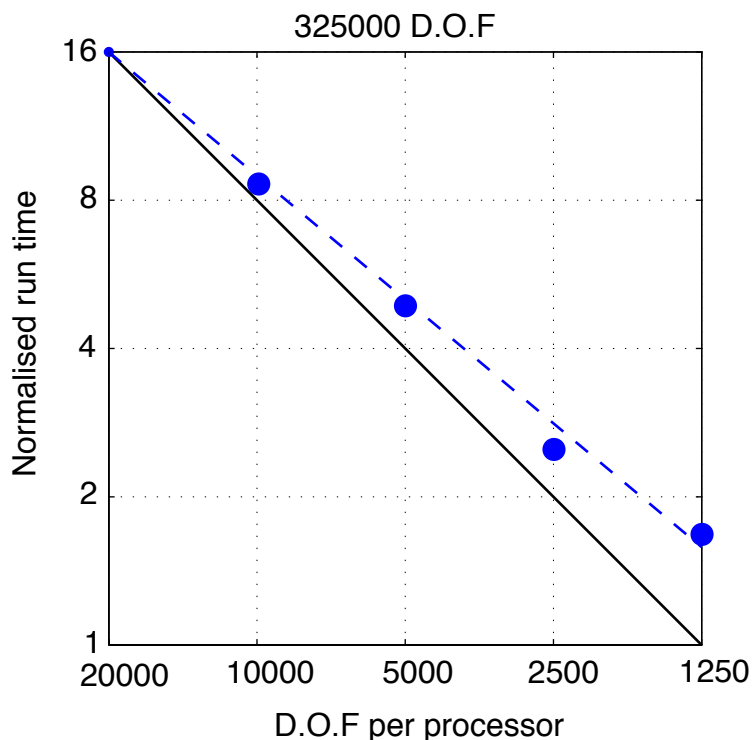


Figure 16: Normalised run time as a function of degrees of freedom (D.O.F) per processor (thus number of processors). The problem size is held constant as the number of processors is increased. Ideally scaling would be perfect, with the run time decreasing by a factor of 2 each time the number of processors is doubled. This figure shown that the code is more than 75% efficient. The scaling study was conducted on REDQUEEN, Oxford Supercomputing Centre. REDQUEEN has 264 dual core Intel Xeon 2.6GHz processors shared equally across 128 computing nodes. Each node has 4GiB RAM. More information about this system can be found at www.oerc.ox.ac.uk/resources/osc.

References

- Ahern, J., and D. Turcotte (1979), Magma migration beneath and ocean ridge, *Earth and Planetary Science Letters*, 45(1), 155–122.
- Albers, M. (2000), A local mesh refinement multigrid method for 3-d convection problems with strongly variable viscosity, *Journal of Computational Physics*, 160(1), 126–150.
- Avendonk, H. V., A. Harding, J. Orcutt, and J. McClain (2001), Contrast in crustal structure across the clipperton transform fault from travel time tomography, *Journal of Geophysical Research*, 106(B6), 10,961–10,981.
- Blackman, D., J. M. Kendall, P. Dawson, H. R. Wenk, D. Boyce, and J. P. Morgan (1996), Teleseismic imaging of subaxial flow at mid-ocean ridges: travelttime effects of anisotropic mineral texture in the mantle, *Geophysical Journal International*, 127, 415–426.
- Bown, J., and R. White (1994), Variation with spreading rate of oceanic crustal thickness and geochemistry, *Earth and Planetary Science Letters*, 121(3-4), 435–449.
- Brunelli, D., M. Seyler, L. Ottolini, and E. Bonatti (2006), Discontinuous melt extraction and weak refertilization of mantle peridotites at the vema lithospheric section (mid-atlantic ridge), *Journal of Petrology*, 47(4), 745–771.
- Carbotte, S., C. Small, and K. Donnelly (2004), The influence of ridge migration on the magmatic segmentation of mid-ocean ridges, *Nature*, 429(6993), 743–746.
- Collier, J., and S. Singh (1998), A seismic inversion study of the axial magma chamber reflector beneath the east pacific rise near 10degreesn, *Geological Society, London, Special Publications*, 148(1), 17–28.
- Davis, E., and J. Karsten (1986), On the cause of the asymmetric distribution of seamounts about the juan de fuca ridge: ridge-crest migration over a heterogeneous asthenosphere, *Earth and Planetary Science Letters*, 79(3-4), 385–396.
- Dick, H., J. Lin, and H. Schouten (2003), An ultraslow-spreading class of ocean ridge, *Nature*, 426(6965), 405–412.
- Forsyth, D., D. Scheirer, S. Webb, L. Dorman, J. Orcutt, A. Harding, D. Blackman, J. Morgan, R. Detrick, Y. Shen, C. Wolfe, J. Canales, D. Toomey, A. Sheehan, S. Solomon, and W. Wilcock (1998), Imaging the deep seismic structure beneath a mid-ocean ridge: The melt experiment, *Science*, 280, 1215–1218.
- Fram, M., and C. Leshner (1993), Geochemical constraints on mantle melting during creation of the north atlantic basin, *Nature*, 363(6431), 712–715.
- Georgen, J. (2008), Mantle flow and melting beneath oceanic ridge–ridge–ridge triple junctions, *Earth and Planetary Science Letters*, 270(3-4), 231–240.

- Hirth, G., and D. Kohlstedt (1996), Water in the oceanic upper mantle: implications for rheology, melt extraction and the evolution of the lithosphere, *Earth and Planetary Science Letters*, 144(1-2), 93–108.
- Holtzman, B., D. Kohlstedt, M. Zimmerman, F. Heidelbach, T. Hiraga, and J. Hustoft (2003), Melt segregation and strain partitioning: Implications for seismic anisotropy and mantle flow, *Science*, 301(5637), 1227–1230.
- Katz, R. (2008), Magma dynamics with the enthalpy method: Benchmark solutions and magmatic focusing at mid-ocean ridges, *Journal of Petrology*, 49(12), 2099–2121.
- Katz, R., M. Spiegelman, and C. Langmuir (2003), A new parameterization of hydrous mantle melting, *Geochem. Geophys. Geosyst.*, 4(9), 1–19.
- Katz, R., M. Spiegelman, and S. Carbotte (2004), Ridge migration, asthenospheric flow and the origin of magmatic segmentation in the global mid-ocean ridge system, *Geophysical Research Letters*, 31, L15,605.
- Kent, G., S. H. A. Singh, M. Sinha, J. Orcutt, P. Barton, R. White, S. Bazin, R. Hobbs, C. Tong, and J. Pye (2000), Evidence from three-dimensional seismic reflectivity images for enhanced melt supply beneath mid-ocean -ridge discontinuities, *Nature*, 406(6796), 614–618.
- Knepley, M., R. Katz, and B. Smith (2006), Developing a geodynamics simulator with PETSc, in *Numerical Solution of Partial Differential Equations on Parallel Computers, Lecture Notes in Computational Science and Engineering*, vol. 51, edited by A. Bruaset and A. Tveito, pp. 413–438, Springer-Verlag.
- Kushiro, I. (2001), Partial melting experiments on peridotite and origin of mid-ocean ridge basalt, *Annual Reviews of Earth and Planetary Sciences*, 29, 71–107.
- Ligi, M., M. Cuffaro, F. Chierici, and A. Calafato (2008), Three-dimensional passive mantle flow beneath mid-ocean ridges: analytical approach, *Geophysical Journal International*, 175(2), 783–805.
- Lin, J., and J. P. Morgan (1992), The spreading rate dependence of three-dimensional mid-ocean ridge gravity structure, *Journal of Geophysical Research*, 19(1), 13–16.
- Macdonald, K., P. Fox, L. Perram, M. Eisen, R. Haymon, S. Miller, S. Carbotte, M. Cormier, and A. Shor (1988), A new view of the mid-ocean ridge from the behaviour of ridge-axis discontinuities, *Nature*, 335(6187), 217–225.
- Magde, L., D. Sparks, and R. Detrick (1997), The relationship between buoyant mantle flow, melt migration, and gravity bull's eyes at the mid-atlantic ridge between 33 °n and 35 °n, *Earth and Planetary Science Letters*, 148(1-2), 59–67.
- McKenzie, D. (1984), The generation and compaction of partially molten rock, *Journal of Petrology*, 25(3), 713–765.
- McKenzie, D., and M. Bickle (1988), The volume and composition of melt generated by extension of the lithosphere, *Journal of Petrology*, 29(3), 625–679.

- Parsons, B., and J. Sclater (1977), An analysis of the variation of ocean floor bathymetry and heat flow with age, *Journal of Geophysical Research*, 82(5), 803–827.
- Rabinowicz, M., S. Rouzo, J. Sempere, and C. Rosemberg (1993), Three-dimensional mantle flow beneath mid-ocean ridges, *Journal of Geophysical Research*, 98(B5), 7851–7869.
- Schouten, H., H. Dick, and K. Klitgord (1987), Migration of mid-ocean-ridge volcanic segments, *Nature*, 326(6116), 835–839.
- Shaw, P. (1992), Ridge segmentation, faulting and crustal thickness in the atlantic ocean, *Nature*, 358, 490–493.
- Singh, S., W. Crawford, H. Carton, T. Seher, V. Combier, M. Cannat, J. Canales, D. Düsünür, J. Escartin, and J. M. Miranda (2006a), Discovery of a magma chamber and faults beneath a mid-atlantic ridge hydrothermal field, *Nature*, 442(7106), 1029–1032.
- Singh, S., A. Harding, G. Kent, M. Sinha, V. Combier, S. Bazin, C. Tong, J. Pye, P. Barton, R. Hobbs, R. White, and J. Orcutt (2006b), Seismic reflection images of the moho underlying melt sills at the east pacific rise, *Nature*, 442(7100), 287–290.
- Sinton, J., and R. Detrick (1992), Mid-ocean ridge magma chambers, *Journal of Geophysical Research*, 97(B1), 197–216.
- S.Karato, and P. Wu (1993), Rheology of the upper mantle: A synthesis, *Science*, 260(5109), 771–778.
- Small, C., and L. Danyushevsky (2003), Plate-kinematic explanation for mid-oceanic-ridge depth discontinuities, *Geology*, 31(5), 399–402.
- Sparks, D., and E. Parmentier (1991), Melt extraction from the mantle beneath spreading centers, *Earth and Planetary Science Letters*, 105(4), 368–377.
- Tegner, C., C. Leshner, M. Larsen, and W. Watt (1998), Evidence from the rare-earth-element record of mantle melting for cooling of the tertiary iceland plume, *Nature*, 395(6702), 591–594.
- Trompert, R., and U. Hansen (1996), The application of a finite volume multigrid method to three-dimensional flow problems in a highly viscous fluid with a variable viscosity, *Geophysical and Astrophysical Fluid Dynamics*, 83, 261–291.
- Turcotte, D., and G. Schubert (2002), *Geodynamics*, second ed., Cambridge.